

## Article

# Differential Fluid Activity in a Single Exhumed Continental Subduction Unit from Local P-T-M(H<sub>2</sub>O) Records of Zoned Amphiboles (North Muya, Eastern Siberia)

Sergei Y. Skuzovatov 

Vinogradov Institute of Geochemistry, Russian Academy of Sciences, 664033 Irkutsk, Russia; skuzovatov@igc.irk.ru

**Abstract:** The behavior of the continental lithosphere in the Alpine-type subduction zones, which primarily depends on its thickness, thermal regime of subduction and availability of fluids/melts, remains an important issue for both metamorphic petrology and geochemistry as well as for resolving the thermomechanical properties of subduction paleo-interfaces. Rehydrated (amphibole- and zoisite-bearing) eclogites from the Neoproterozoic North Muya high-pressure complex (northern Central Asian Orogenic belt, eastern Siberia) were studied in order to assess their peak burial depths, degree of prograde dehydration, and further retrograde hydration extent within a subducted and exhumed continental unit. Three medium-grained eclogites from different localities of HP complex show similarly dry peak assemblages of pyrope-almandine-grossular garnet ( $X_{\text{Grs}}$  up to 0.30,  $X_{\text{Prp}}$  up to 0.25) + Na-rich omphacite (up to 44 mol % of jadeite) + rutile + quartz, which are variably replaced by secondary plagioclase + clinopyroxene  $\pm$  amphibole symplectitic aggregate. The eclogites were subjected to burial at similar peak depths (up to ~17–21 kbar) but different peak temperatures (within ~600–730 °C) with or without notable heating and re-equilibration due to crustal thickening. Variable degrees of exhumation-induced pervasive rehydration led to growth of individual zoned porphyroblastic barroisite-hornblende amphibole ( $^{18}\text{O}/^{16}\text{O} = 0.03\text{--}0.45$ )  $\pm$  zoisite over the primary eclogitic assemblage or after notable thermally-driven development of symplectitic aggregate after omphacite. Amphibole compositions together with the zoisite presence/absence in different samples reflect continuous rehydration by addition of ~0.5–1.5 wt.% at different exhumation conditions, from nearly peak eclogitic P–T (~17–21 kbar) to granulite- and amphibolite-facies depths within the plagioclase stability field (<14 kbar). This diversity most likely required irregular distribution of internally sourced, low-volume, hydrous metamorphic fluid (i.e., from host felsic rocks or metasediments) acting at different depths of the subduction interface. From the performed PTX calculations, I suggest that nearly isochemical (i.e., without any significant modification of the bulk-rock composition other than incorporation of additional H<sub>2</sub>O), retrograde hydration by only at lower- to middle-crust conditions did not significantly influence the density and the rheology of the subducted continental slices due to both (1) a limited abundance of dense metabasic rocks, which are commonly more fluid-rich (e.g., due to chlorite or amphibole alteration), and (2) the initially dry nature of mafic and felsic continental rocks. The limited dehydration and rehydration scales exemplified by the North Muya eclogites and therefore low availability of hydrous metamorphic fluids may have accounted for the high buoyancy of the eclogitic crust and explained the absence of contemporaneous suprasubduction magmatism in the regional context at ca. ~630 Ma.



**Citation:** Skuzovatov, S.Y. Differential Fluid Activity in a Single Exhumed Continental Subduction Unit from Local P-T-M(H<sub>2</sub>O) Records of Zoned Amphiboles (North Muya, Eastern Siberia). *Minerals* **2022**, *12*, 217. <https://doi.org/10.3390/min12020217>

Academic Editor: George M. Gibson

Received: 30 December 2021

Accepted: 5 February 2022

Published: 8 February 2022

**Publisher's Note:** MDPI stays neutral with regard to jurisdictional claims in published maps and institutional affiliations.



**Copyright:** © 2022 by the author. Licensee MDPI, Basel, Switzerland. This article is an open access article distributed under the terms and conditions of the Creative Commons Attribution (CC BY) license (<https://creativecommons.org/licenses/by/4.0/>).

**Keywords:** Central Asian Orogenic belt; Neoproterozoic; subduction; high-pressure metamorphism; eclogites; exhumation; fluid activity; lithospheric rheology

## 1. Introduction

The behavior of the lithosphere in convergence zones is directly governed by its rheology and density [1–4]. These key properties influence the stress release, which occurs

through seismic activity or slower deformations [5]. The rheology and the density of crustal rocks may significantly change during metamorphic modification in the presence of fluid, which is generated in-situ during dehydration of hydrous minerals (e.g., talc or lawsonite) [6,7] or they may be externally sourced [8–10]. A number of studies assumed possible links between fluid generation transport and the distribution of earthquake foci [11,12]. Besides, the presence of hydrous fluids itself is an important kinetic factor, which enhances diffusion, mineral growth, and reactions during metamorphism [13]. Therefore, fluid plays a crucial role in lithospheric modification at both micro- and macro-scale.

The burial and exhumation of high-pressure and ultrahigh-pressure (HP-UHP) rocks in subduction zones are normally coupled with stepped dehydration [14] and further variable rehydration [15–17], which are primarily controlled by a thermal regime (i.e., T/P gradients), timing of convergence, and fluid availability [9,18–20]. The two processes have competing impacts on lithospheric rheology, as they are accompanied by the opposed volume/density changes, corresponding responses to stress introduction, and types of deformations (brittle or ductile). Deeply subducted mafic (eclogitic) crust bear generally low to negligible amounts of volatiles [21,22]. However, their rehydration may occur at a wide range of pressure–temperature conditions, from depths those close to peak burial [15,16,23] to those corresponding to typical retrogression at medium-low P–T during exhumation. Hence, constraining fluid activity and exact P–T conditions of rehydration for different stages of evolution for HP-UHP complexes is crucial for understanding lithospheric behavior in subduction zones, including the estimations of their exhumation rates [24,25]. This behavior is more or less well-known for oceanic-type subduction but remains rather unclear for burial of heterogeneous and primarily felsic subducted continental crust. Here, I present the new results of mineralogical studies and P-T-X modelling of continental-type eclogites from the North Muya block (eastern Siberia, southern framing of the Siberian craton), which highlight the potential differences in exhumation patterns and corresponding fluid impacts on the subducted continental crust on a relatively limited spatial scale. Herein, I intended to check (1) whether the peak eclogite assemblage was completely dry, (2) whether hydrous minerals were present on a whole course of the burial-exhumation evolution, and (3) how well the amphibole composition in “frozen” hydrous assemblages bearing amphibole ± zoisite reproduces the conditions of isochemical (i.e., rehydration-induced only) or metasomatic retrogression.

## 2. Geological Background

The Baikal-Muya Fold Belt (BMFB), located in the northeastern segment of the Central Asian Orogenic Belt (CAOB), is a terrane puzzle formed primarily during Early to Late Neoproterozoic convergence and the corresponding tectonomagmatic activity in the southern periphery of Siberia (Figure 1). The geology and the major stages of the geodynamic evolution of the eastern BMFB have been recently summarized and reported by [26–28]. For decades, the Muya high-grade metamorphic block has been considered an Archean cratonic unit [29–31]. The block comprises the metasedimentary sequences of the Kindikan (lower unit) and the Dzhaltuk series (upper unit), intruded by anatectic granitoids of the Ileir complex [32], and overlain by weakly metamorphosed volcanics, volcano-sedimentary, and terrigenous rocks [29,31,33]. Recent studies confirmed its Neoproterozoic age and suggested its origin is related to the Neoproterozoic reworking of ancient crust [34–37].

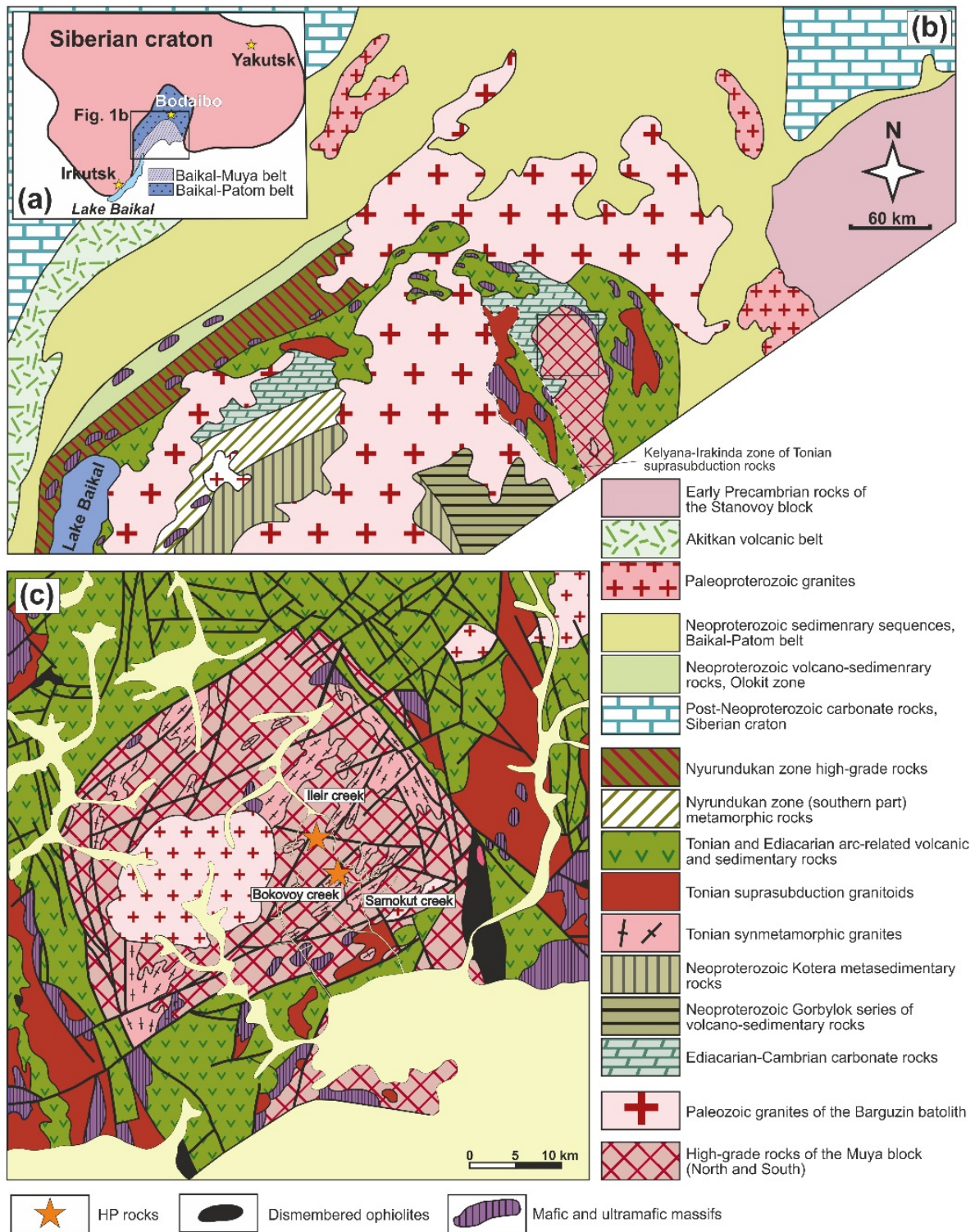


**Figure 1.** Schematic map showing the position of the Baikol-Muya Fold Belt (BMFB) relative to the Siberian craton (a), general structure of the BMFB with key Neoproterozoic complexes (b), and detailed geological structure of the North Muya eclogite-gneiss complex (Cambrian and younger terrigenous and carbonate rocks are not shown) (c).

The eclogites of the North Muya complex (Eastern Siberia) are located within the Early Neoproterozoic metasedimentary and felsic rocks of the BMFB, and occur mostly as meter to tens of meters-scale boudins and lenses within a 10 km wide belt from the Illeir-Samokut pass (marked as a star in Figure 1b), trending northeast for 30 km. A detailed mineralogi-

cal study performed by [38] suggested that eclogites equilibrated under a wide range of pressure and temperature conditions (500–750 °C, minimum pressure of 1.4–1.8 GPa). The Sm-Nd ages of both an eclogite and its host-rock [38], as well as the zircon U-Pb ages [28,35] suggest that the Neoproterozoic metamorphism occurred at approximately ~630 Ma. The eclogites show subduction-related affinity, with large-ion lithophile (LILE) and light rare-earth element (LREE) enrichment and high field-strength element (HFSE) depletion signatures, similar to the exposed plutonic and volcanic rocks of the Early Neoproterozoic (Early Baikalian) subduction setting in the BMFB. Coupled Nd ( $\epsilon_{Nd}(t)$ ) of +6 to –1.4) and Sr ( $^{87}Sr/^{86}Sr$  ratios of 0.705–0.708), along with key trace-element indicators, imply progressive crustal recycling (up to 5–10%) from the Early Precambrian continental rocks to a depleted mantle source or equivalent crustal contribution via intracrustal contamination [28,39]. Mineral  $\delta^{18}O$  data (+3.9–11.5) indicate that the contaminant or recycled crustal substrate might be represented by rocks altered at both low and high-temperature conditions, or result from variable fluid-rock interaction in the subduction channel. Pseudosection modelling of the selected eclogites suggest the Ediacarian high-pressure metamorphic event for different rocks shared a maximum corresponding to 2.5–2.7 GPa with a variable temperature range (560–760 °C), reflecting their potential relation to distinct slices of the subducted crust. The estimated metamorphic conditions for both the burial and exhumation of rocks indicate a continental subduction setting with a warm geotherm (~20–25 °C/kbar). These conditions resulted from the continental subduction of the Baikal-Muya composite structure beneath the relatively thin and immature overlying arc lithosphere of southern Siberia.

### 3. Sample and Methods

For this study, I selected three eclogite samples from the two eclogite-facies locations within the North Muya high-pressure complex. Two eclogites are from the Ileir area (Mu-93-21, Mu-93-71), where relatively fresh eclogites were reported in detail by [38]. One sample was taken from the Samokut area, for which new mineralogical, isotopic, thermobarometric and geochronological data were recently reported by [28]. Both locations have eclogite blocks and boudins entrained within felsic gneisses and metasedimentary schists; the Samokut area lacks fresh eclogites, while symplectitic (i.e., with omphacite completely replaced by clinopyroxene/amphibole + plagioclase symplectite), variably amphibolized eclogites are abundant.

The data on mineral composition of rock-forming and accessory phases of eclogites were acquired using a JEOL Superprobe JXA8200 electron-microprobe analyzer (JEOL Ltd., Tokyo, Japan) equipped with five wavelength-dispersive (WDX) spectrometers, using a beam size of 2  $\mu$ m, a beam current of 15 nA, and an accelerating voltage of 20 kV. The set of natural and synthetic standards used for calibration included albite (Na), pyrope for Al, K-feldspar (K), diopside (Si, Ca, Mg), olivine (Si, Mg, Fe), garnet (Si, Al, Fe, Mn), rutile (Ti), and chromite (Cr, Fe). The on-peak and background counting times for each element were 10 s each, and analytical errors were typically within from 0.01 (for minor elements with the contents close to corresponding detection limits) to 0.1–0.2 wt%. The calculation of mineral structural formulae for garnet, omphacite, and zoisite was undertaken using the CALCMIN software (version 35-07-19) [40], and the formulation of [41] was used for amphiboles. SEM mapping of selected thin section areas was done using a Tescan MIRA 3 scanning electron microscope (TESCAN, Brno, The Czech Republic).

Thermodynamic calculations using the pseudosection method were performed using the Perple\_X software package (version 6.7.6) [42] and the improved database of [43] (version 2002). The following models were used in the calculations: Gt(WPH) for garnet [44], Chl(HP) for chlorite and Ep(HP) for epidote [43], Omph (GHP) for clinopyroxene [45], Amph (DPW) for amphibole [46], and the CORK X(CO<sub>2</sub>) model for fluids [47].

## 4. Results

### 4.1. Petrography and Mineral Chemistry

Three selected eclogite samples from two distinct areas of the HP complex share a few textural and mineralogical similarities. All three are fine- to medium-grained rocks, composed of pinkish garnet (generally within 50–200  $\mu\text{m}$  in size), omphacite and/or fine-grained plagioclase + diopside  $\pm$  amphibole symplectite, porphyroblastic greenish to brownish amphibole up to 0.5–1 cm in size, as well as accessory rutile and quartz. Garnets in all three rocks are rather poor in mineral inclusions, mostly represented by quartz and rutile. Overall, the eclogites show similar abundances of garnet (generally approximately ~15%) and similar styles of post-peak rehydration, which is associated with the formation of porphyroblastic amphiboles over the primary garnet + omphacite + rutile + quartz assemblage. Despite these similarities, there are several specific features that distinguish the three eclogites. The eclogite sample Mu-13-22 (Samokut locality) lacks visible omphacite, which is completely replaced by plagioclase + diopside  $\pm$  amphibole symplectite and has rare biotite + ilmenite symplectitic intergrowths, with both types of symplectites overgrown by amphibole porphyroblasts (Figure 2a–c). In the eclogite sample Mu-93-21 (Ileir locality), both primary omphacite and its replacement products plagioclase + diopside are observed. The most specific feature for this eclogite sample is the presence of matrix zoisite and its inclusions in porphyroblastic amphiboles in some areas of the thin section (Figure 2d–f). Noteworthy, thin sections areas rich in zoisite have the highest degree of omphacite replacement by symplectite, as previously noticed by [38]. The eclogite sample Mu-93-71 (Ileir locality) displays the best preservation of omphacite among the studied rocks and—on the opposite—the minimum spread of symplectite, whereas amphibole porphyroblasts overgrow garnet, omphacite, and rutile (Figure 2g–i). Overall, based on the observed peak and garnet inclusion assemblages, as well as on their relationships with hydrous minerals, I suggest that (1) prograde evolution of eclogites likely occurred at relatively fluid-deficient conditions (fine-grained garnet with no inclusions of hydrous minerals), and (2) peak assemblage of all three eclogites was represented by dry garnet + omphacite + rutile  $\pm$  quartz assemblages.

EPMA data for major mineral phases for the three samples (representative compositions are provided in Table 1) revealed rather homogeneous composition of garnets within the three samples (Figure 3a). Both Mu-93-21 ( $\text{Alm}_{41-44}\text{Grs}_{20-24}\text{Prp}_{32-37}\text{Sps}_1$ ) and Mu-93-71 ( $\text{Alm}_{56-58}\text{Grs}_{21-25}\text{Prp}_{16-19}\text{Sps}_{1-2}$ ) eclogites exhibit only limited variations between individual garnet grains, with no clear zonation patterns observed for each analyzed grain (Figure 3a). Relative to these two eclogites, the Mu-13-22 sample displays a more notable scatter of individual garnet compositions ( $\text{Alm}_{41-58}\text{Grs}_{21-30}\text{Prp}_{20-25}\text{Sps}_{1-2}$ ), which is the most significant for almandine and grossular proportions. Quantitative profiles through selected grains did not recover a single zonation pattern or show calculated proportions of almandine, grossular and rarer pyrope are fluctuating throughout the crystal. Omphacite in Mu-93-21 and Mu-93-71 eclogites show jadeite molar proportions up to 42% and 41%, respectively, and variable but uncertain aegirine (acmite) ( $\text{Fe}^{3+}$ ) component (Figure 3b). Diopside-augite pyroxene from symplectites varies in both calculated  $\text{Fe}^{3+}$  contribution and jadeite proportion, but it generally shows less than 16% of jadeite. Zoisite in the Mu-93-21 eclogite is uniform in composition, showing  $\text{Fe}_2\text{O}_3$  mainly within 1.62–2.16% and  $X_{\text{Fe}^{3+}}$  of 0.03–0.04, with only rare Fe-enriched rims ( $X_{\text{Fe}^{3+}}$  up to 0.13). The latter may correspond to late epidote overgrowths.

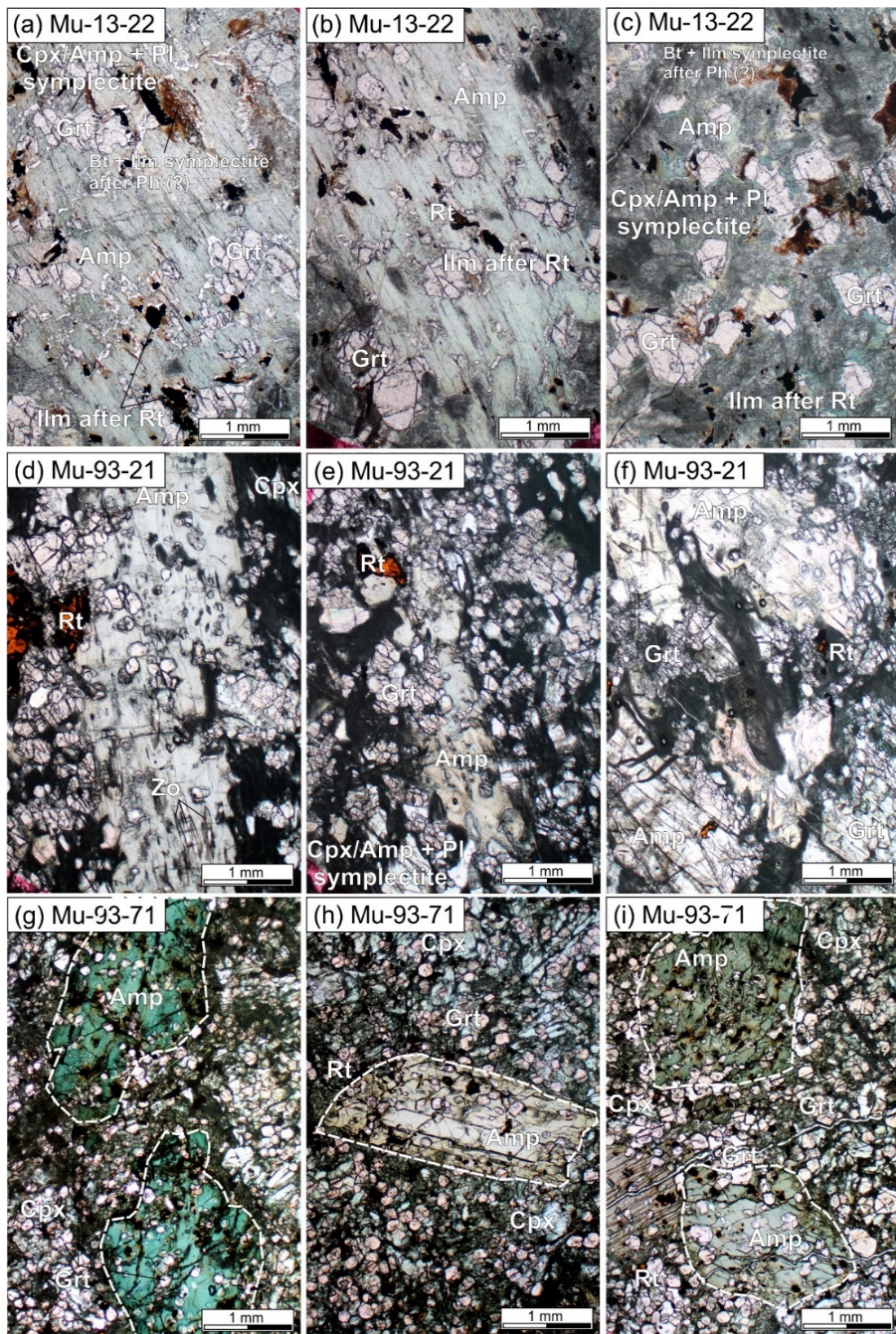


**Figure 2.** Representative transmitted-light microphotographs showing petrography of the North Muya eclogites at thin section sites with porphyroblastic amphibole, used further for analyses and calculations: (a–c) sample Mu-13-22, (d–f) samples Mu-93-21, and (g–i) sample Mu-93-71. Grt: garnet; Cpx: clinopyroxene; Rt: rutile; Amp: amphibole; Pl: plagioclase; Bt: biotite; Ph: phengite; Ilm: ilmenite; Zo: zoisite.

**Table 1.** Representative mineral composition in eclogites from the North Muya HP complex.

| Component                      | Sample Mu-93-21 |             |           |             |       |       |       |       |       |      |  |
|--------------------------------|-----------------|-------------|-----------|-------------|-------|-------|-------|-------|-------|------|--|
|                                | Grt 1 (c)       | Grt 1 (rim) | Grt 2 (c) | Grt 2 (rim) | Omp 1 | Omp 2 | Amp 1 | Amp 2 | Amp 3 | Zo   |  |
| SiO <sub>2</sub>               | 39.9            | 40.3        | 39.4      | 39.8        | 55.9  | 56.4  | 50.6  | 47.0  | 49.0  | 39.3 |  |
| TiO <sub>2</sub>               | 0.05            | 0.00        | 0.07      | 0.04        | 0.02  | 0.13  | 0.23  | 0.34  | 0.16  | 0.01 |  |
| Al <sub>2</sub> O <sub>3</sub> | 23.1            | 23.8        | 23.2      | 23.0        | 11.0  | 11.4  | 10.9  | 13.1  | 11.4  | 32.9 |  |
| Cr <sub>2</sub> O <sub>3</sub> | 0.01            | 0.05        | 0.00      | 0.08        | 0.06  | 0.06  | 0.00  | 0.00  | 0.00  | 0.04 |  |
| FeO                            | 20.1            | 19.5        | 20.3      | 20.5        | 2.66  | 2.54  | 5.86  | 7.98  | 8.61  | 1.54 |  |
| MnO                            | 0.41            | 0.38        | 0.42      | 0.42        | 0.01  | 0.01  | 0.03  | 0.05  | 0.04  | 0.00 |  |
| MgO                            | 9.28            | 8.96        | 8.94      | 8.96        | 9.63  | 9.73  | 17.4  | 16.1  | 18.1  | 0.16 |  |
| CaO                            | 8.49            | 8.77        | 8.61      | 8.34        | 14.0  | 14.1  | 8.03  | 8.32  | 7.93  | 22.7 |  |
| Na <sub>2</sub> O              | 0.05            | 0.00        | 0.03      | 0.03        | 6.51  | 6.44  | 3.72  | 3.64  | 2.92  | 0.01 |  |
| K <sub>2</sub> O               | 0.00            | 0.00        | 0.00      | 0.00        | 0.00  | 0.01  | 0.25  | 0.32  | 0.19  | 0.01 |  |
| Sum                            | 101.4           | 101.7       | 101.0     | 101.1       | 99.9  | 100.8 | 97.1  | 97.1  | 98.4  | 96.7 |  |
| Si                             | 5.92            | 5.98        | 5.85      | 5.94        | 1.97  | 1.97  | 7.06  | 6.67  | 6.84  | 3.01 |  |
| Ti                             | 0.01            | 0.00        | 0.01      | 0.00        | 0.00  | 0.00  | 0.02  | 0.04  | 0.02  | 0.00 |  |
| Al                             | 4.04            | 4.16        | 4.06      | 4.05        | 0.46  | 0.47  | 1.80  | 2.19  | 1.87  | 2.97 |  |
| Cr                             | 0.00            | 0.01        | 0.00      | 0.01        | 0.00  | 0.00  | 0.00  | 0.00  | 0.00  | 0.00 |  |
| Fe <sup>2+</sup>               | 2.50            | 2.42        | 2.53      | 2.55        | 0.04  | 0.07  | 0.47  | 0.64  | 0.78  | 0.00 |  |
| Fe <sup>3+</sup>               | 0.00            | 0.00        | 0.00      | 0.00        | 0.03  | 0.01  | 0.22  | 0.31  | 0.22  | 0.10 |  |
| Mn                             | 0.05            | 0.05        | 0.05      | 0.05        | 0.00  | 0.00  | 0.00  | 0.01  | 0.00  | 0.00 |  |
| Mg                             | 2.05            | 1.98        | 1.98      | 2.0         | 0.51  | 0.51  | 3.62  | 3.40  | 3.76  | 0.02 |  |
| Ca                             | 1.35            | 1.39        | 1.37      | 1.34        | 0.53  | 0.53  | 1.20  | 1.26  | 1.19  | 1.86 |  |
| Na                             | 0.01            | 0.00        | 0.01      | 0.01        | 0.45  | 0.44  | 1.01  | 1.00  | 0.79  | 0.00 |  |
| K                              | 0.00            | 0.00        | 0.00      | 0.00        | 0.00  | 0.00  | 0.04  | 0.06  | 0.03  | 0.00 |  |

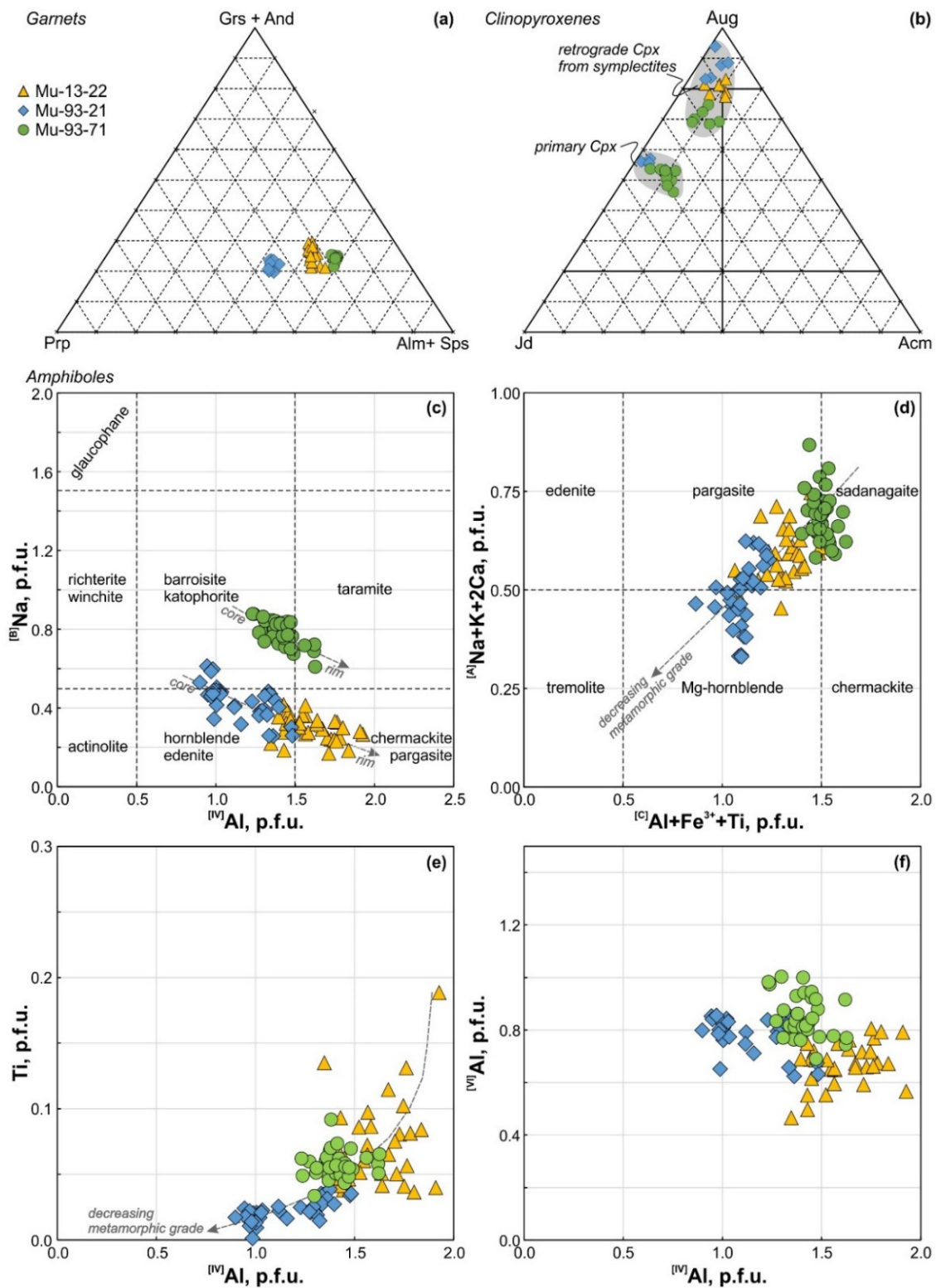
| Component                      | Sample Mu-93-71 |             |           |             |       |       |       |       |       |  |
|--------------------------------|-----------------|-------------|-----------|-------------|-------|-------|-------|-------|-------|--|
|                                | Grt 1 (c)       | Grt 1 (rim) | Grt 2 (c) | Grt 2 (rim) | Omp 1 | Omp 2 | Amp 1 | Amp 2 | Amp 3 |  |
| SiO <sub>2</sub>               | 38.8            | 38.8        | 38.2      | 38.8        | 56.1  | 56.2  | 45.0  | 47.4  | 44.1  |  |
| TiO <sub>2</sub>               | 0.14            | 0.08        | 0.07      | 0.00        | 0.03  | 0.22  | 0.51  | 0.46  | 0.60  |  |
| Al <sub>2</sub> O <sub>3</sub> | 22.2            | 22.4        | 22.4      | 22.1        | 10.5  | 10.3  | 12.5  | 13.1  | 14.1  |  |
| Cr <sub>2</sub> O <sub>3</sub> | 0.03            | 0.02        | 0.04      | 0.01        | 0.02  | 0.04  | 0.00  | 0.00  | 0.00  |  |
| FeO                            | 26.4            | 26.4        | 25.9      | 26.3        | 5.23  | 5.94  | 11.7  | 12.0  | 13.8  |  |
| MnO                            | 0.60            | 0.68        | 0.63      | 0.67        | 0.03  | 0.03  | 0.04  | 0.05  | 0.06  |  |
| MgO                            | 4.41            | 4.66        | 4.46      | 4.49        | 8.55  | 8.01  | 12.9  | 12.0  | 11.9  |  |
| CaO                            | 8.71            | 8.31        | 8.61      | 8.92        | 13.3  | 12.4  | 7.64  | 7.21  | 8.50  |  |
| Na <sub>2</sub> O              | 0.00            | 0.07        | 0.00      | 0.12        | 6.74  | 7.58  | 4.47  | 5.03  | 4.38  |  |

Table 1. Cont.

|                  |       |       |       |       |       |       |      |      |      |
|------------------|-------|-------|-------|-------|-------|-------|------|------|------|
| K <sub>2</sub> O | 0.00  | 0.00  | 0.00  | 0.00  | 0.01  | 0.00  | 0.56 | 0.59 | 0.57 |
| Sum              | 100.5 | 101.3 | 100.3 | 101.4 | 100.6 | 100.7 | 95.4 | 97.9 | 97.9 |
| Si               | 6.00  | 5.96  | 5.93  | 5.96  | 1.99  | 1.98  | 6.61 | 6.76 | 6.37 |
| Ti               | 0.02  | 0.01  | 0.01  | 0.00  | 0.00  | 0.01  | 0.06 | 0.05 | 0.07 |
| Al               | 4.04  | 4.06  | 4.10  | 4.00  | 0.44  | 0.43  | 2.16 | 2.21 | 2.40 |
| Cr               | 0.00  | 0.00  | 0.00  | 0.00  | 0.00  | 0.00  | 0.00 | 0.00 | 0.00 |
| Fe <sup>2+</sup> | 3.42  | 3.39  | 3.36  | 3.38  | 0.11  | 0.06  | 0.84 | 1.01 | 1.06 |
| Fe <sup>3+</sup> | 0.00  | 0.00  | 0.00  | 0.00  | 0.05  | 0.11  | 0.60 | 0.42 | 0.61 |
| Mn               | 0.08  | 0.09  | 0.08  | 0.09  | 0.00  | 0.00  | 0.01 | 0.01 | 0.01 |
| Mg               | 1.02  | 1.07  | 1.03  | 1.03  | 0.45  | 0.42  | 2.81 | 2.56 | 2.56 |
| Ca               | 1.44  | 1.37  | 1.43  | 1.47  | 0.50  | 0.47  | 1.20 | 1.01 | 1.06 |
| Na               | 0.00  | 0.02  | 0.00  | 0.04  | 0.46  | 0.52  | 1.27 | 1.39 | 1.23 |
| K                | 0.00  | 0.00  | 0.00  | 0.00  | 0.00  | 0.00  | 0.11 | 0.11 | 0.10 |

| Component                      | Sample Mu-13-22 |             |           |             |       |       |       |       |       |
|--------------------------------|-----------------|-------------|-----------|-------------|-------|-------|-------|-------|-------|
|                                | Grt 1 (c)       | Grt 1 (rim) | Grt 2 (c) | Grt 2 (rim) | Cpx 1 | Cpx 2 | Amp 1 | Amp 2 | Amp 3 |
| SiO <sub>2</sub>               | 39.0            | 39.0        | 38.6      | 38.8        | 53.1  | 53.6  | 45.8  | 46.1  | 42.5  |
| TiO <sub>2</sub>               | 0.01            | 0.06        | 0.00      | 0.04        | 0.16  | 0.11  | 0.38  | 0.40  | 0.37  |
| Al <sub>2</sub> O <sub>3</sub> | 23.0            | 22.6        | 22.7      | 22.9        | 6.04  | 5.26  | 13.0  | 12.9  | 16.0  |
| Cr <sub>2</sub> O <sub>3</sub> | 0.00            | 0.02        | 0.01      | 0.01        | 0.04  | 0.01  | 0.00  | 0.00  | 0.00  |
| FeO                            | 23.7            | 23.2        | 22.8      | 23.7        | 6.68  | 6.71  | 11.4  | 11.6  | 13.0  |
| MnO                            | 0.51            | 0.57        | 0.49      | 0.51        | 0.10  | 0.10  | 0.09  | 0.09  | 0.07  |
| MgO                            | 6.37            | 5.74        | 5.90      | 6.13        | 11.6  | 12.0  | 14.9  | 14.6  | 12.9  |
| CaO                            | 8.61            | 9.67        | 9.86      | 9.16        | 19.0  | 19.7  | 8.69  | 8.52  | 10.2  |
| Na <sub>2</sub> O              | 0.00            | 0.05        | 0.11      | 0.03        | 3.04  | 2.57  | 2.99  | 2.99  | 2.95  |
| K <sub>2</sub> O               | 0.00            | 0.00        | 0.00      | 0.00        | 0.00  | 0.01  | 0.60  | 0.63  | 0.82  |
| Sum                            | 101.2           | 100.9       | 100.7     | 101.7       | 99.8  | 100.1 | 98.0  | 98.0  | 98.9  |
| Si                             | 5.91            | 5.95        | 5.91      | 5.92        | 1.94  | 1.95  | 6.54  | 6.57  | 6.09  |
| Ti                             | 0.00            | 0.01        | 0.00      | 0.01        | 0.00  | 0.00  | 0.04  | 0.04  | 0.04  |
| Al                             | 4.10            | 4.07        | 4.06      | 4.07        | 0.26  | 0.23  | 2.18  | 2.18  | 2.70  |
| Cr                             | 0.00            | 0.00        | 0.00      | 0.00        | 0.00  | 0.00  | 0.00  | 0.00  | 0.00  |
| Fe <sup>2+</sup>               | 3.01            | 2.97        | 2.90      | 3.00        | 0.14  | 0.16  | 0.89  | 0.90  | 0.93  |
| Fe <sup>3+</sup>               | 0.00            | 0.00        | 0.00      | 0.00        | 0.07  | 0.04  | 0.47  | 0.49  | 0.63  |
| Mn                             | 0.07            | 0.08        | 0.07      | 0.07        | 0.00  | 0.00  | 0.01  | 0.01  | 0.01  |
| Mg                             | 1.44            | 1.31        | 1.34      | 1.38        | 0.63  | 0.66  | 3.16  | 3.10  | 2.75  |
| Ca                             | 1.40            | 1.58        | 1.61      | 1.48        | 0.74  | 0.77  | 1.33  | 1.30  | 1.57  |
| Na                             | 0.00            | 0.02        | 0.03      | 0.01        | 0.21  | 0.18  | 0.83  | 0.83  | 0.82  |
| K                              | 0.00            | 0.00        | 0.00      | 0.00        | 0.00  | 0.00  | 0.11  | 0.11  | 0.15  |

Grt—garnet (c—grain center, rim—grain rim); Omp—omphacite; Cpx—clinopyroxene from symplectite; Amp—amphibole; Zo—zoisite.



**Figure 3.** Compositional graphs for major rock-forming minerals of the studied eclogites, including garnet (a), clinopyroxene (omphacite and diopside-augite from symplectitic aggregates) (b), and amphiboles (c–f). Grs: grossular; And: andradite; Alm: almandine; Sps: spessartine; Aug: augite; Jd: jadeite; Acm: acmite.

Porphyroblastic amphiboles in the three samples show significant compositional variations, some of which have apparent core-to-rim distribution (Figures 3c–f and 4). Generally,

they show different enrichment in Na and its proportion as  $^{[B]}Na$  (with a difference of up to 0.2–0.3 formula units), as well as a significant range of  $^{[IV]}Al$  (Figure 3c), which classify the Na-rich amphiboles in the Mu-93-71 eclogite as barroisites (4.38–5.51 wt% of  $Na_2O$ ), and more Na-poor amphiboles from Mu-93-21 (2.18–3.91 wt% of  $Na_2O$ ) and Mu-13-22 eclogite (1.65–3.17 wt% of  $Na_2O$ ) as hornblendes/edenites [48]. The same  $^{[B]}Na$ - $^{[IV]}Al$  systematics exhibits clear negative core-rim correlation, with the cores enriched in Na and showing a lower Si-to-Al substitution scale (Figure 4). According to the newer classification scheme of [49], the same amphiboles are classified primarily as Na-richer pargasites and Na-poorer Mg-hornblendes (Figure 3d), without a clear core-rim dependence probably due to the uncertainty of  $Fe^{3+}$  estimations and a possible effect of Ti. More specifically, the most Ti-enriched amphiboles from the Mu-13-22 eclogite display the widest variations of Ti proportion (Figure 3e), whereas a narrower version is observed in Ti-poorer porphyroblasts from the other two eclogites. While amphiboles in the Mu-93-21 eclogite reveal a clear negative dependence between the calculated  $^{[VI]}Al$  and  $^{[IV]}Al$  mole proportions, amphibole porphyroblasts from the two other samples show the absence of  $^{[VI]}Al$ - $^{[IV]}Al$  correlation (Figure 3f). Along with the zoned distribution of Na, the most contrasting distribution patterns in amphiboles are recovered from Fe and Mg zonation (Figure 5). All three eclogite samples show a similar decrease in Mg toward porphyroblast rims (core-rim variations up to  $\sim 0.5$  formula units of  $Mg^{2+}$ ) at a decreased or nearly homogeneous distribution of Fe (Figure 6), associated with Si-to-Al replacement in tetrahedral positions (Figure 5).

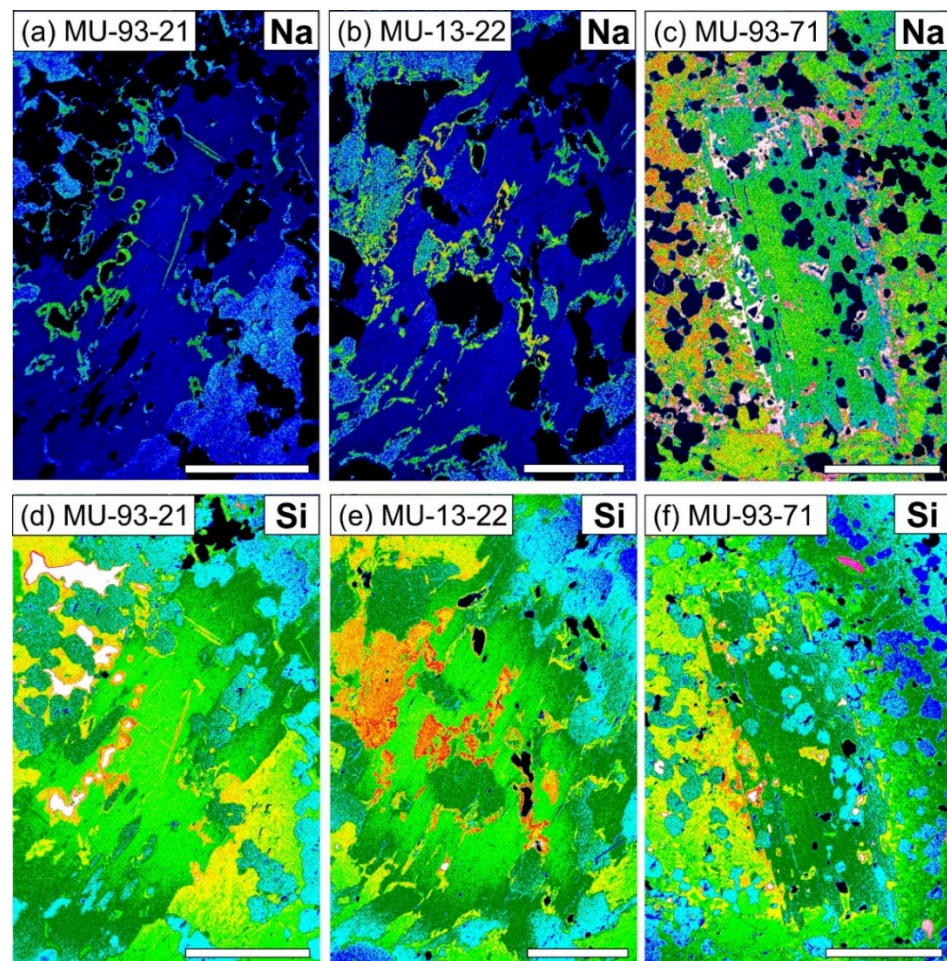


**Figure 4.** SEM maps for Na and Si distribution in porphyroblastic amphiboles. The scale bar for is equal to 1 mm. (a–c) Na; (d–f) Si.

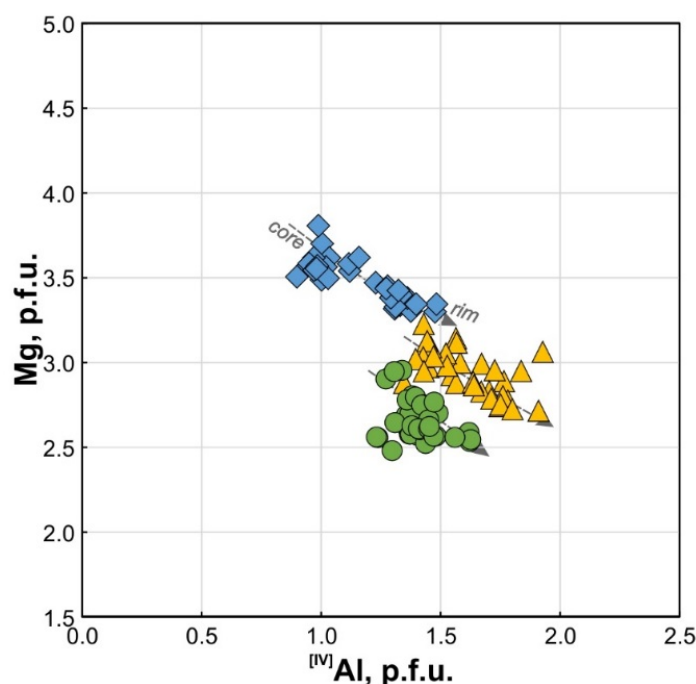


**Figure 5.** Additional compositional graphs for the analyzed amphiboles showing Mg–Al relations in the core–rim reference.

According to the newer classification scheme of [49], the same amphiboles are classified primarily as Na-richer pargasites and Na-poorer Mg-hornblendes (Figure 3d), without a clear core–rim dependence probably due to the uncertainty of  $\text{Fe}^{3+}$  estimations and a possible effect of Ti. More specifically, the most Ti-enriched amphiboles from the Mu-13-22 eclogite display the widest variations of Ti proportion (Figure 3e), whereas a narrower range is observed in Ti-poorer porphyroblasts from the other two eclogites. While amphiboles in the Mu-93-21 eclogite reveal a clear negative dependence between the calculated  $[\text{VI}]\text{Al}$  and  $[\text{IV}]\text{Al}$  mole proportions, amphibole porphyroblasts from the two other samples show the absence of  $[\text{VI}]\text{Al}$ – $[\text{IV}]\text{Al}$  correlation (Figure 3f). Along with the obviously zoned distribution of Na, the most contrasting distribution patterns in amphiboles are recovered from Fe and Mg zonation (Figure 5). All three eclogite samples show a similar decrease in Mg towards porphyroblast rims (core–rim variations up to  $\sim 0.5$  formula units of  $\text{Mg}^{2+}$ ) at a more moderate decrease or nearly homogeneous distribution of Fe (Figure 6), associated with progressive Si-to-Al replacement in tetrahedral positions (Figure 5).

#### 4.2. Prograde and Peak Pressure—Temperature Modelling

To recover the possible prograde and peak metamorphic conditions, including prograde garnet crystallization, the XRF data for the contents of the major oxides were used as an effective bulk composition (EBC) (Table 2). The latter were taken as undifferentiated, but required two important modifications, with all  $\text{K}_2\text{O}$  and  $\text{P}_2\text{O}_5$  removed from the EBCs.  $\text{K}_2\text{O}$  was not included in the calculations based on the K-feldspar and white mica absence in the Mu-93-21 and Mu-93-71 eclogites, and only negligible biotite presence in the Mu-13-22 sample. The total CaO proportionally adjusted to account for the contribution of  $\text{P}_2\text{O}_5$  from apatite. Thus, the MnNCFMASHT(O) ( $\text{MnO}$ – $\text{Na}_2\text{O}$ – $\text{CaO}$ – $\text{FeO}$ – $\text{MgO}$ – $\text{Al}_2\text{O}_3$ – $\text{SiO}_2$ – $\text{H}_2\text{O}$ –(O)) system has been used for calculations. Different  $X_{\text{Fe}^{3+}}$  values were adopted previously for the PTX calculations modelling the evolution of mafic eclogites, ranging from zero to 0.35. However, Li et al. [50] reported that changing the  $X_{\text{Fe}^{3+}}$  range has a subtle influence on the pseudosection results. Assuming that the  $\text{Fe}^{3+}$  content of minerals, calculated from their structural formulas, may be uncertain, the values of  $X_{\text{Fe}^{3+}}$  were set on the basis of  $P$ – $X_{\text{Fe}^{3+}}$  space analysis at different temperature sections, which best reproduce the observed compositions of rock-forming phases. The  $\text{H}_2\text{O}$ -fluid was originally assumed to be in

excess for constraining the prograde subsolidus and peak metamorphic parameters. Lastly, given the previous P–T estimates for the North Muya eclogites [28,38], I used the ranges of 15–30 kbar and 550–750 °C for equilibrium calculations representing potential peak P–T conditions of dry eclogites.

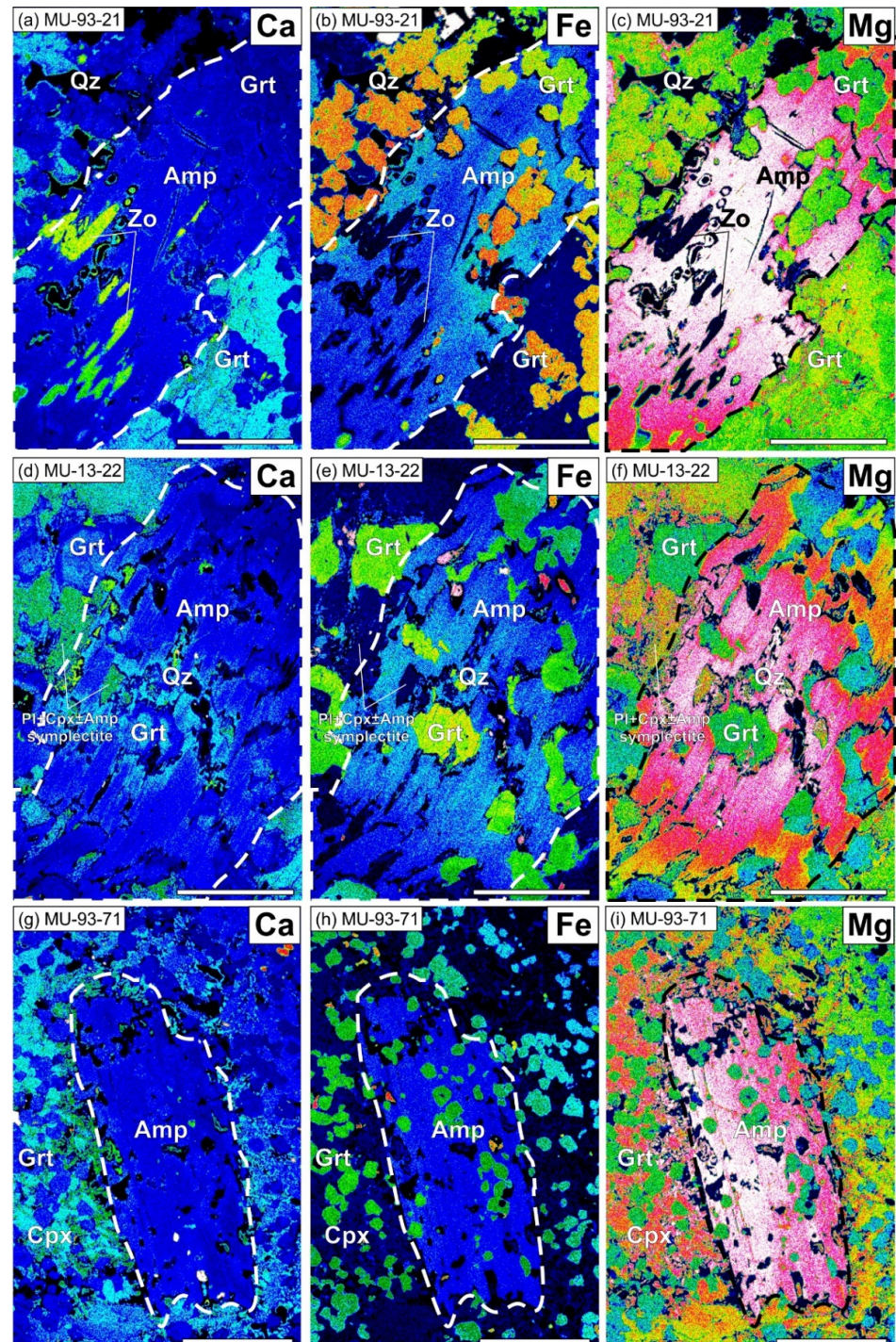


**Figure 6.** Selected SEM maps for Ca, Mg, and Fe content distribution in porphyroblastic amphiboles and adjacent/included phases of the Mu-93-21 (a–c), Mu-13-22 (d–f), and Mu-93-71 (g–i) eclogites. The scale bar for is equal to 1 mm. Grt: garnet; Cpx; clinopyroxene; Qz: quartz; Zo: zoisite; Amp: amphibole; Pl: plagioclase.

Table 2. Bulk rock compositions used for PTX pseudosection modelling.

| Component                      | Sample Mu-93-21 |         |      | Sample Mu-93-71 |         |      | Sample Mu-13-22 |         |      |
|--------------------------------|-----------------|---------|------|-----------------|---------|------|-----------------|---------|------|
|                                | EBC1            | av. Grt | EBC2 | EBC1            | av. Grt | EBC2 | EBC1            | av. Grt | EBC2 |
| SiO <sub>2</sub>               | 47.8            | 40.0    | 49.3 | 48.0            | 38.6    | 49.4 | 48.2            | 39.0    | 49.7 |
| TiO <sub>2</sub>               | 1.23            | 0.06    | 1.43 | 2.65            | 0.09    | 3.04 | 1.98            | 0.06    | 2.27 |
| Al <sub>2</sub> O <sub>3</sub> | 15.8            | 23.2    | 14.6 | 14.2            | 22.3    | 13.0 | 14.8            | 22.6    | 13.7 |
| FeO                            | 11.6            | 20.1    | 10.1 | 13.3            | 26.0    | 11.9 | 13.3            | 23.6    | 11.7 |
| Fe <sub>2</sub> O <sub>3</sub> | 0.00            | 0.00    | 0.00 | 0.77            | 0.00    | 0.36 | 0.00            | 0.00    | 0.00 |
| MnO                            | 0.20            | 0.41    | 0.17 | 0.20            | 0.64    | 0.14 | 0.24            | 0.52    | 0.20 |
| MgO                            | 9.30            | 9.13    | 9.35 | 6.31            | 4.52    | 6.59 | 6.63            | 5.86    | 6.75 |
| CaO                            | 11.2            | 8.14    | 11.8 | 10.7            | 8.62    | 11.0 | 11.2            | 9.14    | 11.6 |
| Na <sub>2</sub> O              | 2.76            | 0.04    | 3.25 | 3.97            | 0.04    | 4.57 | 3.55            | 0.04    | 4.08 |
| H <sub>2</sub> O               | exc.            |         |      | exc.            |         |      | exc.            |         |      |

EBC1—non-differentiated effective bulk rock composition obtained from the XRF data; av. Grt—average composition of garnets cores in a sample; EBC2—differentiated effective bulk rock composition obtained by subtracting the average garnet core composition (see description in the text); and exc.—excess of H<sub>2</sub>O fluid used for modelling.

Given the above assumed fluid-deficient and hence most likely medium-T prograde-to-peak mineral assemblages, isopleths of garnet corresponding to the observed almandine-pyrope-grossular and jadeite ( $X_{\text{Jd-in-Omp}}$  up to 0.42) proportions in the Mu-93-21 eclogite ( $X_{\text{Alm}} = 0.44\text{--}0.43$ ,  $X_{\text{Prp}} > 0.33$ ,  $X_{\text{Grs}} = 0.21\text{--}0.24$ ) resemble an amphibole + garnet + omphacite + rutile + quartz stability field in a wide range of P–T conditions within  $\sim 625\text{--}725$  °C and  $\sim 19\text{--}25$  kbar (Figure 7a). However, assuming limited and continuous garnet growth, the location of isopleths best correspond to a more limited range of P–T conditions at 19–21 kbar and  $\sim 675\text{--}725$  °C. To add, omphacite compositions may be consistent with its earlier formation at less significant depths. As seen from P–T reconstructions, the isopleth shape is subparallel to amphibole-out reaction line, and both  $X_{\text{Grs-in-Grt}}$  and  $X_{\text{Jd-in-Omp}}$  do not change significantly along the boundary between fields of hydrous, amphibole-bearing and dry amphibole-free assemblages, thus not allowing more precise constraining of the peak P–T. However, it may be outlined that (1) garnet growth occurred at relatively high P–T and it involved amphibole and/or zoisite dehydration reactions; (2) eclogitic precursor was most likely H<sub>2</sub>O-poor to avoid garnet growth at earlier prograde conditions; and (3) the dry garnet + omphacite + rutile + quartz eclogite may have experienced notable heating up to  $\sim 730$  °C during partial decompression following peak burial, as deduced from the average garnet-omphacite thermometry data [38].

Similar P–T reconstructions for the Mu-93-71 eclogite required a no-zero  $\text{Fe}^{3+}/\Sigma\text{Fe}$  ratio for the undifferentiated EBC, as the EPMA data for omphacite and amphibole exhibit both a high overall #Fe and a high recalculated  $\text{Fe}^{3+}$  proportion (for instance, see Figure 3b for omphacite). To ensure a correct reconstructed rutile-ilmenite relationship (no ilmenite observed) but also to avoid any bias in garnet-omphacite compositions ( $X_{\text{Alm}} = 0.56\text{--}0.58$ ,  $X_{\text{Prp}} = 0.16\text{--}0.19$ ,  $X_{\text{Grs}} = 0.21\text{--}0.25$ ,  $X_{\text{Jd-in-Omp}}$  up to 0.45), I applied  $\text{Fe}^{3+}/\Sigma\text{Fe}$  of 0.05. The calculations yielded the most probable garnet nucleation conditions and garnet-omphacite coexistence at P–T similar to the above ( $\sim 590\text{--}625$  °C and  $\sim 18\text{--}21$  kbar), but at lower temperatures and without any evidence of heating produced re-equilibration, as highlighted by garnet-omphacite temperatures (Figure 8a).

Finally, for the symplectitic eclogite Mu-13-22, which did not preserve primary omphacite and showed more variable garnet compositions ( $X_{\text{Alm}} = 0.48\text{--}0.56$ ,  $X_{\text{Prp}} = 0.20\text{--}0.25$ ,  $X_{\text{Grs}} = 0.21\text{--}0.30$ ), the P–T estimations yielded the most probable garnet growth conditions at only slightly lower pressures and similar temperatures ( $\sim 640\text{--}690$  °C and  $\sim 17\text{--}19$  kbar) within an amphibole stability field and thus likely through amphibole decomposition reactions, similar to those for the above eclogites (Figure 9a). The reconstructed omphacite composition at these P–T conditions shows up to 42 mol % of jadeite, which also resembles well the composition of omphacite from the two other eclogites. Nonetheless, both pyrope-almandine ratios and textural evidence of the extensive symplectite development after a dry omphacite-bearing assemblage indicates significant re-equilibration at

higher temperatures. Additional P–T sections for the same EBC, yielded dry plagioclase-bearing garnet-clinopyroxene-rutile-quartz assemblage stable at the same pressure range (~17–19 kbar) but starting from ~770 °C and extending towards ~850 °C, which support the effect of temperature increase up to granulite facies.

#### 4.3. Retrograde Evolution of Eclogites and Fluid Activity Modelling

For further constraints onto peak/retrograde evolution and potential effect of the early garnet crystallization onto EBC, including fluid overprint impacts, the effective bulk compositions of all three samples have been modified by subtracting the contribution of garnet cores. This approach implies that most of the garnet volume was not involved in the late-stage mineral re-equilibration reactions. Garnet core contribution was estimated by combining the spatial analysis of SEM elemental maps with the average composition of central parts of garnets (from 25 to 45 measurements per sample). The analysis of SEM maps for several areas in each section revealed similarly moderate proportions of garnet varying within ~15–20% for all three eclogites. Hence, to constrain the possible effect of garnet fractionation onto EBC, for each sample, I obtained fractionated EBCs by subtracting the early garnet composition corresponding to 13 (samples Mu-13-22 and Mu-93-71) to 15% of sample volume (sample Mu-93-21), respectively. Unlike some examples, where retrogression conditions were particularly well constrained [17], such data for the North Muya eclogites are lacking. The gradual exhumation-related change of retrograde assemblages is more sensitive to decompression by 5–10 kbar rather than cooling by ~100–150 °C (Figures 7–9). Therefore, P– $M_{H_2O}$  sections were composed further in a ~10–20 kbar range, resembling decompression from peak high-pressure conditions to lower-pressure, amphibolite or epidote-amphibolite facies at the same temperatures, which were assumed based on garnet-omphacite thermometry [38] or are most probable from P–T pseudosection modelling (see above).

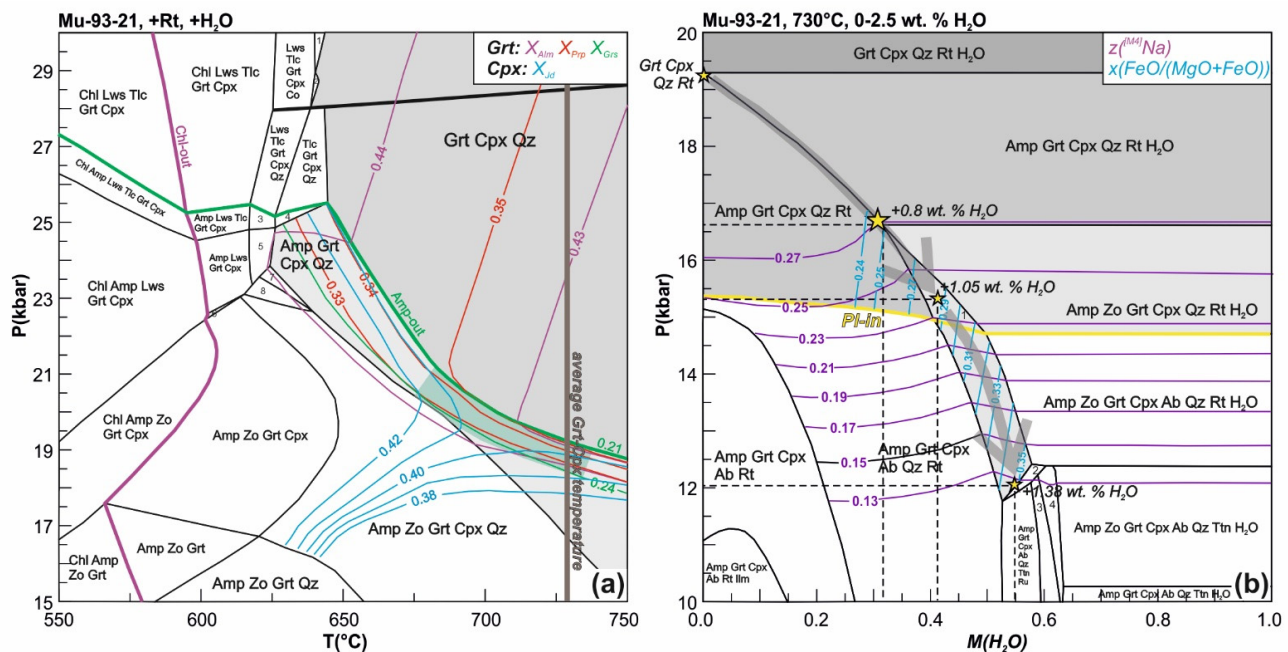


**Figure 7.** P–T pseudosection modelling results showing the most probable prograde garnet growth conditions in the sample Mu-93-21 defined by almandine-pyrope-grossular-jadeite isopleths (a), and P– $M_{H_2O}$  model of retrograde evolution during decompression and fluid introduction using the amphibole composition (b). Grt: garnet; Cpx: clinopyroxene; Amp: amphibole; Qz: quartz; Co: coesite; Rt: rutile; Lws: lawsonite; Tlc: talc; Zo: zoisite; Chl: chlorite; Ttn: titanite; Ab: albite.

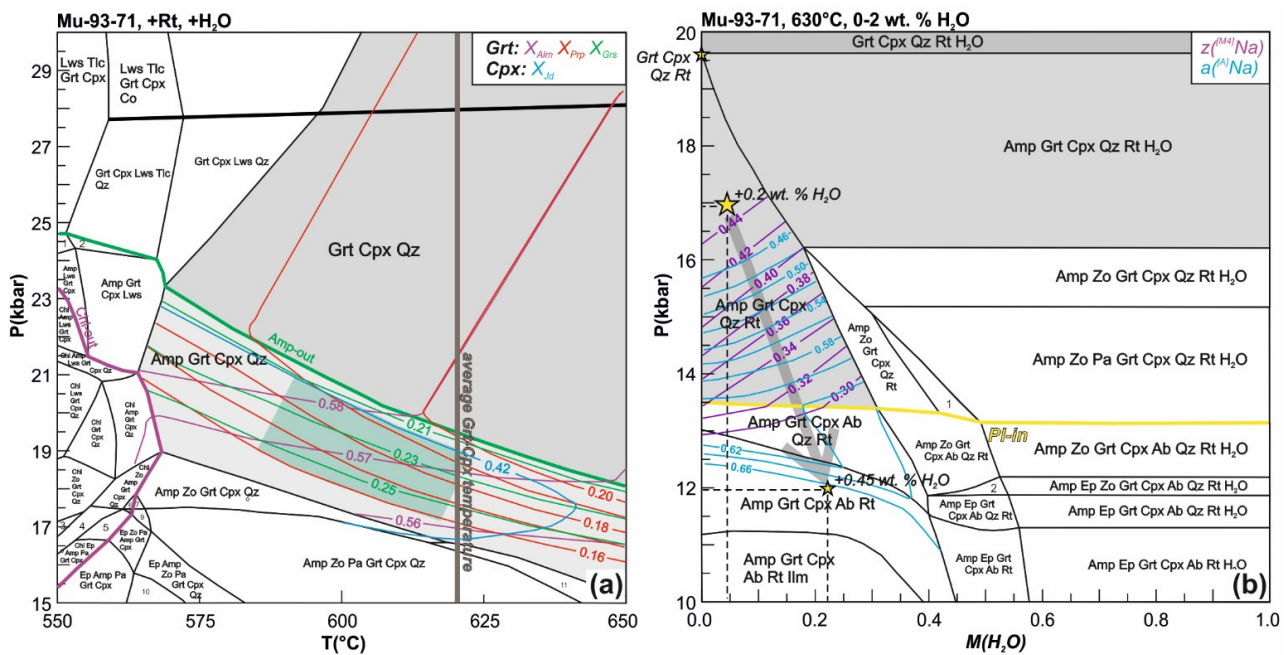


**Figure 8.** P–T pseudosection modelling results showing the most probable prograde garnet growth conditions in the sample Mu-93-71 defined by almandine-pyrope-grossular-jadeite isopleths (a), and P–M<sub>H2O</sub> model of retrograde evolution during decompression and fluid introduction using the amphibole composition (b). Grt: garnet; Cpx; clinopyroxene; Amp: amphibole; Qz: quartz; Co: coesite; Rt: rutile; Lws: lawsonite; Tlc: talc; Zo: zoisite; Chl: chlorite; Ttn: titanite; Pa: paragonite; Ep: epidote; Ab: albite; Ilm: ilmenite.

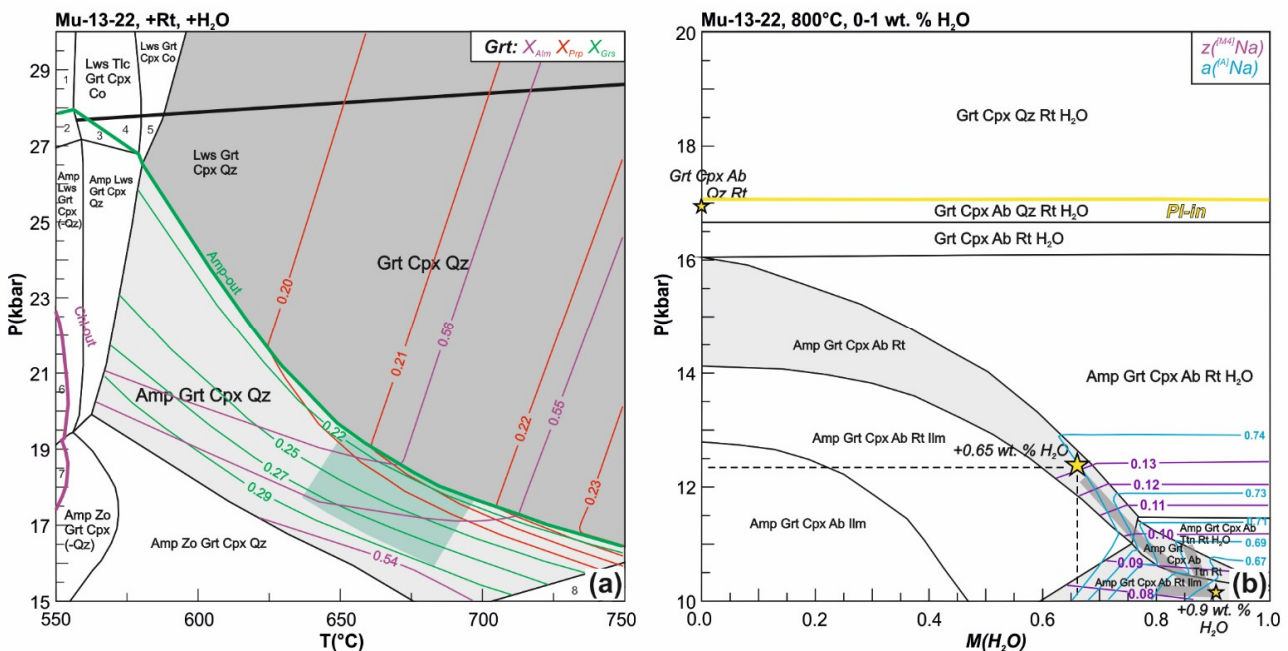


**Figure 9.** P–T pseudosection modelling results showing the most probable prograde garnet growth conditions in the sample Mu-13-22 defined by almandine-pyrope-grossular-jadeite isopleths (a), and P–M<sub>H2O</sub> model of retrograde evolution during decompression and fluid introduction using the amphibole composition (b). Grt: garnet; Cpx; clinopyroxene; Amp: amphibole; Qz: quartz; Co: coesite; Rt: rutile; Lws: lawsonite; Tlc: talc; Zo: zoisite; Chl: chlorite; Ttn: titanite; Pa: paragonite; Ep: epidote; Ab: albite; Ilm: ilmenite.

As no  $\text{Fe}^{3+}$  was used for the initial bulk-rock composition of the Mu-93-21 sample, for further fluid activity calculations, I similarly imply all Fe as  $\text{Fe}^{2+}$ , which, however, contradicts the medium-to-high  $\text{Fe}^{3+}/\Sigma\text{Fe}$  ratio calculated from the EPMA data. As  $\text{Fe}^{3+}$  contribution affects the estimation of some key chemical components (e.g.,  $^{[M4]}\text{Na}$  and respective glaucophane proportion), I also assessed the possible effects of this simplification onto  $\text{P-M}_{\text{H}_2\text{O}}$  estimations through a set of additional  $\text{P-M}_{\text{H}_2\text{O}}$  sections at variable, non-zero  $\text{Fe}^{3+}$  proportions in both amphiboles and EBCs. The use of  $\text{Fe}^{3+}$ -free amphibole recalculation underestimates the glaucophane ( $^{[M4]}\text{Na}$ ) proportion by  $\sim 0.03\text{--}0.04$ , when that translates to systematic pressure underestimation by just  $\sim 1.0\text{--}1.5$  kbar. This indicates the relatively limited effect of this simplification onto calculation in a reduced eclogite with a low real  $\text{Fe}^{3+}/\Sigma\text{Fe}$ . To avoid potential biases in calculation, amphibole compositions were correspondingly corrected on an  $\text{Fe}^{3+}$ -free basis using formulations of [41]. The re-calculated values of the amphibole  $^{[B]}\text{Na}$  occupancy (mainly within 0.12–0.27) and #Fe ( $\text{FeO}/(\text{FeO}+\text{MgO})$  in wt%) (0.24–0.37) are consistent with continuous amphibole growth within the amphibole–zoisite stability field from high pressure ( $\sim 16.5$  kbar) towards plagioclase stability field (down to 12 kbar) (Figure 7b). The corresponding  $\text{H}_2\text{O}$  addition to the dry eclogitic assemblages gradually grows within a narrow range from 0.8 to 1.4 wt%.

Unlike the sample above, for the Mu-93-71 eclogite, the calculations should involve an addition of  $\text{Fe}^{3+}$ , which was initially required to account for the compositions of rock-forming garnet and omphacite. Hence, a similar iron oxidation state value ( $\text{Fe}^{3+}/\Sigma\text{Fe}$  of 0.05) was assumed at the first stage. Preliminary formula recalculations revealed a much more prominent underestimation of the amphibole  $^{[M4]}\text{Na}$  occupancy (by  $\sim 0.08\text{--}0.10$ ), when omitting  $\text{Fe}^{3+}$ , which also precludes using all Fe as  $\text{Fe}^{2+}$  for modelling. Relevant  $^{[M4]}\text{Na}$  occupancy (0.30–0.44) for the given EBC ( $\sim 13\%$  of volume occupied by garnet) are reproduced in a reasonable, amphibole + garnet + omphacite + quartz + rutile field at  $\sim 13.5\text{--}19$  kbar and below 0.8 wt%  $\text{H}_2\text{O}$  added to the EBC. However, predicted equilibrium amphiboles should have lower #Fe values (0.31–0.44) and total Fe contents than the observed. Multiple reasonable, higher, or lower recalculations omitted garnet proportions as a major Fe-bearing phase (from the initial undifferentiated EBC to 10–20% of garnet-occupied volume subtracted) showed no significant effects onto reconstructed amphibole #Fe. A detailed check-up on the reconstructed phase compositions revealed preferential Fe enrichment of co-existing omphacite, whereas the hornblende remains Fe-poor all the way through a  $\text{P-T}$  of interest. I may conclude that, in case of the Mu-93-71 eclogite,  $\text{Mg}/\text{Fe}$  and potentially  $\text{Fe}^{2+}/\text{Fe}^{3+}$  relations are more complex and they cannot be an instrument for unequivocal constraint on the  $\text{P-T}$  of hydration. Using the speciation of Na, which seems to behave more statically, for instance, as  $a = ^{[A]}\text{Na}$ , I obtained more reliable constraints on the conditions of rehydration, which range from 17 kbar to as low as 12 kbar but with remarkably low  $\text{H}_2\text{O}$ -fluid addition (within 0.2–0.4 wt%) (Figure 8b).

The last, Mu-13-22 eclogite sample, which is characteristic of a distinct exhumation regime of its hosting gneiss–schist domain, had undergone heating up to  $\sim 750\text{--}850$  °C while staying at dry (fluid-deficient) conditions. Given the textural evidence of porphyroblastic amphibole displaying poikilitic inclusions of plagioclase + clinopyroxene  $\pm$  amphibole symplectite, the eclogite avoided fluid retrogression at HP conditions and was subjected to only limited rehydration within the plagioclase stability field (i.e., below  $\sim 16$  kbar).  $\text{P-M}_{\text{H}_2\text{O}}$  sections constructed at relevant temperatures of peak heating (for instance, Figure 9b shows the results for 800 °C) assuming all Fe as  $\text{Fe}^{2+}$  revealed reasonable amphibole compositions ( $^{[M4]}\text{Na} = 0.03\text{--}0.13$ ,  $^{[A]}\text{Na} = 0.52\text{--}0.75$ , #Fe = 0.40–0.50) starting from 13 kbar towards even lower “crustal” pressures and with the addition of 0.65–0.9 wt% of  $\text{H}_2\text{O}$  to EBC (Figure 9b). Furthermore, lower-pressure and more  $\text{H}_2\text{O}$ -enriched conditions are needed to account for the minimum  $^{[M4]}\text{Na}$  at maximum  $^{[A]}\text{Na}$  and #Fe values obtained from the sample. Here, the calculation again implied zero  $\text{Fe}^{3+}/\Sigma\text{Fe}$ , whereas, similar to that in the Mu-93-71 eclogite, recalculated amphibole compositions show a moderate to high contribution of  $\text{Fe}^{3+}$ . The reconstructed amphibole growth conditions are consistent with the observed abundant replacement of rutile by ilmenite.

## 5. Discussion

### 5.1. Sources and Scales of Potential Uncertainties in Characterizing Prograde-To-Peak P–T Calculations

Along with the uncertainties of EPMA measurements and possible simplifications from using particular solid-solution models (especially that of amphibole and clinopyroxene), the P–T pseudosection approach used in this study involved several additional approximations, of which the following three are the most crucial:

- (1) Selecting the EBCs consistent with real equilibrated sample volumes;
- (2) Selecting the appropriate  $\text{Fe}^{3+}/\text{Fe}^{2+}$ , which affects stability of some phases (e.g., zoisite);
- (3) Assuming the equilibrium nature of amphibole relative to garnet-free bulk rock volume;
- (4) The effect of diffusional re-equilibration of dry eclogitic (garnet + omphacite) assemblages.

Here, the conventionally used, XRF-measured, bulk-rock compositions were applied as EBCs, stemmed from (1) relatively homogeneous composition of primary garnet and omphacite, and (2) textural homogeneity on a scale of thin sections (including garnet proportions throughout the sections). For instance, as mentioned above, several additional PTX re-calculations were performed, which did not show any significant effect of the garnet cutout (within 0–20 vol%) onto reconstructed amphibole chemistries. This confirms the absence of garnet/pyroxene porphyroblasts limits the fractionation of equilibrium rock volumes and thus allows P–T estimations via modelling, which uses non-differentiated whole-rock compositions.

Using an appropriate  $\text{Fe}^{3+}/\text{Fe}^{2+}$  may be much more crucial for EBCs, as it generally controls the equilibrium content of jadeite/acmite in omphacite and pyrope/almandine ratios in garnet, and hence pressure estimations as well as  $\text{Mg}^{2+}$ - $\text{Fe}^{2+}$  exchange-based equilibria calculations. This is particularly significant for characterizing prograde-to-peak history of eclogites due to (1) the absence of low- to medium-grade hydrous minerals correlated to garnet zoning, and (2) non-intersecting or subparallel compositional isopleths. In case of garnet in the North Muya eclogites,  $X_{\text{Grs}}$  isopleths may indicate a gradual growth via amphibole-out and/or zoisite-out reactions [51] at relatively fluid-deficient conditions (with  $\text{H}_2\text{O}$  source in amphibole and/or zoisite only), whereas slow  $\text{Ca}^{2+}$ -in-garnet diffusion is unlikely to be affected by any post-peak thermal disturbance [52]. On the contrary, heating-induced diffusion successfully imprints  $\text{Mg}^{2+}$ - $\text{Fe}^{2+}$  exchange towards more Mg-rich composition of eclogitic garnet for high-temperature eclogites (as in case of Mu-93-21 and Mu-13-22 samples), and it accounts for the uncertainty in constructing almandine-pyrope isopleths.

Though medium-to-high  $\text{Fe}^{3+}/\text{Fe}^{2+}$  ratios in omphacite commonly stem from EPMA analyses, only the use of zero to low  $\text{Fe}^{3+}/\text{Fe}^{2+}$  in EBCs for all three eclogitic samples revealed the reproducibility of the measured and calculated omphacite compositions. Even higher  $\text{Fe}^{3+}/\text{Fe}^{2+}$  ratios were recalculated for amphibole, which were inherited from omphacite or—in some cases—resemble even more oxidized compositions ( $\text{Fe}^{3+}/\Sigma\text{Fe}$  up to ~0.5). The first scenario (with zero  $\text{Fe}^{3+}/\Sigma\text{Fe}$ ) was a priori favored in this study, based on multiple re-calculations in order to reproduce most closely the observed garnet-omphacite chemistries. Although intrusive continental and arc rocks may display a range of initial  $\text{Fe}^{3+}/\Sigma\text{Fe}$  [53], variations within a 0.0–0.1 range yield negligible effect onto calculations. Low  $\text{Fe}^{3+}$  content in zoisite, which is a favorable carrier of  $\text{Fe}^{3+}$  in the given metabasic assemblage of the Mu-93-21 eclogite, is another potential indicator of overall low bulk  $\text{Fe}^{3+}/\Sigma\text{Fe}$  ratios.

To resume, while a complete, internally-consistent solution for these issues may be impossible, the results obtained for the three texturally similar eclogite from the North Muya HP complex show both good reproducibility of phase compositions (primary water-free silicates and retrograde hydrous phases) and consistency between the determined P–T–X parameters and textural evidence of rehydration conditions.

### 5.2. Styles of Retrograde Evolution and Rehydration Conditions of High-Pressure Assemblages

The major driving force of retrograde metamorphism is rehydration of rocks, completely or partially dehydrated on a course of prograde evolution, by in-situ generated or external H<sub>2</sub>O-rich fluid, which is favored over a simple and gradual transition from high-grade to lower-grade equilibrium assemblages [54–57]. Regardless of the fluid source and volume, reactive consumption of a H<sub>2</sub>O-fluid leads to inhibition of further retrograde transformations and kinetic “freezing” of the current H<sub>2</sub>O-bearing assemblage [13,58]. Thus, the preserved hydrous mineral assemblage should reflect (1) preferential or even complete chemical inheritance from its dehydrated (dry) precursor, (2) the amount of available fluid consumed during rehydration reactions, and (3) characteristic conditions of rehydration itself.

Medium- to fine-grained eclogites from the North Muya HP complex are texturally homogeneous and comparable in terms of the inferred burial depths (~17–21 kbar, which translates to ~50–60 km), which depend primarily on their similar position at the thickened continental crust during the culmination of subduction metamorphism (~630 Ma; [28,38]). Their particular thermal conditions of burial–exhumation (~590–730 °C, this study) and fluid regime of exhumation were somewhat different, e.g., because of the specific crustal thickness of the subducted continental slices and availability of hydrous fluid en route to the surface during exhumation. Also, while some porphyroblastic eclogites from the same HP location were initially low-temperature and H<sub>2</sub>O-rich (i.e., lawsonite, talc, or clinozoisite-bearing) and dehydrated significantly during prograde to retrograde evolution [28], medium-grained eclogites were likely H<sub>2</sub>O-poor (with only amphibole and/or zoisite present and decomposed on a prograde stage) and had a distinct style of exhumation. More specifically, Mu-93-21 and Mu-93-71 eclogites experienced complete dehydration followed by continuous re-hydration from high-pressure to elevated-medium pressure (plagioclase stability) conditions (~12–17 kbar). In this case, retrograde modification of the eclogites were primarily controlled by the amount of available H<sub>2</sub>O-fluid. Supplying only limited amount (~0.2–0.5 wt%) of H<sub>2</sub>O led to preferential amphibole porphyroblast growth in the Mu-93-71 eclogite, whereas a bit more significant amount of hydrous fluid (~0.8–1.4 wt.% of H<sub>2</sub>O) produced zoisite–amphibole assemblage at similar conditions. Although the precise construction of the prograde P–T evolution of eclogites was not possible, this work shows that the prograde history was fluid-deficient until fluid introduction occurred at the onset of exhumation. This is particularly supported by variable omphacite preservation and development of plagioclase + clinopyroxene ± amphibole symplectite. The latter process is generally enhanced by hydrous fluid availability [59], which was higher in the Mu-93-21 amphibole–zoisite bearing, H<sub>2</sub>O-rich eclogite, but more limited in the Mu-93-71, H<sub>2</sub>O-depleted eclogite. Hence, retrograde hydration in both samples might be apparently initiated at pressures higher than that of typical omphacite destabilization (above ~14–16 kbar).

In contrast, while showing similar minimum peak P–T estimates (not less than ~640–690 °C and ~17–19 kbar), the Mu-13-22 eclogite experienced evident heating of ~770–850 °C, which led to partial diffusional Mg-Fe<sup>2+</sup> redistribution (as seen from garnet zonation and pyrope-almandine isopleths) and omphacite destabilization with only partial decompression. Thus, for some eclogites and their host crustal sections, peak pressures did not associate with peak temperatures, which is typical for collisional orogens [60]. The assumed peak assemblage and its dry nature during exhumation en route up to depths corresponding to ~13 kbar and—more probably—even lower pressures indicate primarily dry conditions during prograde-to-retrograde evolution, whereas only a limited amount of fluid (~0.6–0.9 wt.% of H<sub>2</sub>O). This inferred notable heating at relatively fluid-deficient conditions resulted from the maximum crustal thickening due to stacking of a series of tectonic slices after the termination of subduction-accretion events [61]. Noteworthy, for the garnet-omphacite eclogite Mu-93-71, [38] also reported relatively high equilibrium temperatures (an average of ~730 °C), which is seemingly much higher than expected from thermodynamic modelling (Figure 8a), but eventually not enough to cause profound

decomposition of omphacite at relevant pressures. The stability of primary, high-pressure omphacite and garnet instead of their replacement may be a key reason for a degree of bias in reconstructed amphibole chemistries (e.g., its #Fe and  $\text{Fe}^{3+}/\Sigma\text{Fe}$ ).

### 5.3. Implications to Fluid Effects onto Buoyancy of the Continental Crust and Crust-Mantle Interactions

The studied North Muya eclogites were subjected to burial at similar peak depths (up to ~19–21 kbar) but different peak temperatures (within ~600–730 °C) with or without notable heating and re-equilibration due to crustal thickening. Variable degrees of exhumation-induced pervasive rehydration (~0.2–1.5 wt% of  $\text{H}_2\text{O}$  added to bulk rocks) led to continuous growth of individual zoned porphyroblastic barroisite-hornblende amphibole  $\pm$  zoisite, which record variable but generally low fluid activities and thus availability in a wide range of pressures, from near-peak (~17–21 kbar) to those well beyond omphacite and rutile stability fields (<10 kbar). P–T constraints obtained from hydrous assemblages imply that low-volume, hydrous fluid introduced into the corresponding exhumed crustal sections were distributed rather irregularly, and they were most likely internally sourced, i.e., derived from eclogite dehydration or from that of the host felsic rocks. Hydrous fluid derived from subduction metamorphism generally migrates along the subduction channel or moves upward through the mantle wedge [11,62,63], whereas their lateral migration is limited [64,65]. However, this process should be more suppressed in case of the dry, predominantly felsic continental crust that favors only limited fluid migration and, therefore, an internal (host-rock) fluid source. From the performed P–T–X calculations, I suggest that nearly isochemical (i.e., without any significant modification of the bulk-rock composition other than incorporation of additional  $\text{H}_2\text{O}$ ), retrograde hydration by only at lower- to middle-crust conditions did not significantly influence the density and the rheology of the subducted continental slices due to both (1) a limited abundance of dense metabasic and commonly more fluid-rich rocks (e.g., due to chlorite or amphibole alteration), and (2) the initially dry nature of mafic and felsic continental rocks. The limited dehydration and rehydration scales exemplified by the North Muya eclogites and therefore low availability of hydrous metamorphic fluid may have accounted for the high buoyancy of eclogitic crust but also may explain the absence of contemporaneous suprasubduction magmatism in the regional context at ca. ~630 Ma.

## 6. Conclusions

Three medium-grained, rehydrated (amphibole- and zoisite-bearing) eclogites from the Neoproterozoic North Muya high-pressure complex (northern Central Asian Orogenic belt, eastern Siberia) were studied in order to assess their peak burial depths, degree of prograde dehydration, and extent of further retrograde hydration within a subducted and exhumed continental unit. Given the observed petrographic observations, mineral composition data, and thermodynamic modelling results, the most important outcomes are as follows:

- (1) The eclogites were subjected to burial at similar peak depths (at least up to ~19–21 kbar) but different peak temperatures (within ~600–730 °C) with or without notable heating and re-equilibration due to crustal thickening.
- (2) A variable degree of exhumation-induced pervasive rehydration led to growth of individual zoned porphyroblastic barroisite-hornblende amphibole  $\pm$  zoisite over the primary eclogitic assemblage or after notable heating-driven development of symplectitic aggregate after omphacite. Amphibole compositions together with the zoisite presence/absence in different samples reflect continuous rehydration by addition of ~0.2–1.5 wt% of  $\text{H}_2\text{O}$ , which controlled both the growth of hydrous minerals and the degree of omphacite decomposition.
- (3) Different exhumation conditions were revealed, from nearly peak eclogitic P–T (~17–18 kbar) to granulite- and amphibolite-facies depths within the plagioclase stability field (<14 kbar), as well as variable thermal regimes (with or without post-peak heating), that may reflect the effect of crustal thickness. These differences most likely

reflect irregular distribution of internally sourced, low-volume, hydrous metamorphic fluid (i.e., from host felsic rocks or metasediments) acting at different depths of the subduction interface.

- (4) Nearly isochemical (i.e., without any significant modification of the bulk-rock composition other than incorporation of additional H<sub>2</sub>O), retrograde hydration at lower- to middle-crust conditions did not significantly influence the density and the rheology of the subducted continental slices due to both (1) limited abundance of dense metabasic and commonly more fluid-rich (e.g., due to chlorite or amphibole alteration), and (2) the initially dry nature of mafic and felsic continental rocks. The limited dehydration and rehydration scales exemplified by the North Muya eclogites and therefore low availability of hydrous metamorphic fluid may have accounted for high buoyancy of the eclogitic crust and explained the absence of contemporaneous suprasubduction magmatism in the regional context at ca. ~630 Ma.

**Funding:** SEM/EPMA studies of eclogites were supported by the Russian Science Foundation (Grant 21-77-10038). Thermodynamic modelling was performed within the framework of the Russian Federation President Grant (MK-67.2020.5).

**Acknowledgments:** The thin section collection used for selecting representative hydrous eclogites was in part provided by Vladislav Shatsky, whose general assistance and advisory are acknowledged. I am also grateful to Olga Belozerova and Anastasiya Chueshova (IGC SB RAS) for their assistance in SEM and EPMA studies. The effort of three anonymous referees and the editorial remarks of Yican Liu are also appreciated.

**Conflicts of Interest:** The author declares no conflict of interest.

## References

- Burov, E. Rheology and strength of the lithosphere. *Marine Petrol. Geol.* **2011**, *28*, 1402–1443. [[CrossRef](#)]
- Chen, W.-P.; Molnar, P. Focal depths of intracontinental and intraplate earthquakes and their implications for the thermal and mechanical properties of the lithosphere. *J. Geophys. Res. Atmosph.* **1983**, *88*, 4183–4214. [[CrossRef](#)]
- Clark, M.-K.; Royden, L.-H. Topographic ooze: Building the eastern margin of Tibet by lower crustal flow. *Geology* **2000**, *28*, 703–706. [[CrossRef](#)]
- von Blanckenburg, F.H.; Davies, J.H. Slab breakoff: A model for syncollisional magmatism and tectonics in the Alps. *Tectonics* **1995**, *14*, 1320–1331. [[CrossRef](#)]
- Jamtveit, B.; Petley-Ragan, A.; Incel, S.; Dunkel, K.-G.; Aupart, C.; Austrheim, H.; Corfu, F.; Menegon, L.; Renard, F. The effects of earthquakes and fluids on the metamorphism of the lower continental crust. *J. Geophys. Res. Solid Earth* **2019**, *124*, 7725–7755. [[CrossRef](#)]
- Zheng, Y.F.; Fu, B.; Gong, B.; Li, L. Stable isotope geochemistry of ultrahigh pressure metamorphic rocks from the Dabie-Sulu orogen in China: Implications for geodynamics and fluid regime. *Earth-Sci. Rev.* **2003**, *62*, 105–161. [[CrossRef](#)]
- Vitale Brovarone, A.; Groppo, C.; Hetenyi, G.; Compagnoni, R.; Malavielle, J. Coexistence of lawsonite-bearing eclogite and blueschist: Phase equilibria modelling of Alpine Corsica metabasalts and petrological evolution of subducting slabs. *J. Metamorph. Geol.* **2011**, *29*, 583–600. [[CrossRef](#)]
- Carson, C.J.; Clarke, G.; Powell, R. Hydration of eclogite, Pam Peninsular, New Caledonia. *J. Metamorph. Geol.* **2000**, *18*, 79–90. [[CrossRef](#)]
- van der Straaten, F.; Schenk, V.; John, T.; Gao, J. Blueschist-facies rehydration of eclogites (Tian Shan, NW-China): Implications for fluid–rock interaction in the subduction channel. *Chem. Geol.* **2008**, *255*, 195–219. [[CrossRef](#)]
- van der Straaten, F.; Halama, R.; John, T.; Schenk, V.; Hauff, F.; Andersen, N. Tracing the effects of high-pressure metasomatic fluids and seawater alteration in blueschist-facies overprinted eclogites: Implications for subduction channel processes. *Chem. Geol.* **2012**, *292–293*, 69–87. [[CrossRef](#)]
- Hacker, B.R.; Abers, G.A.; Peacock, S.M. Subduction factory 1. Theoretical mineralogy, densities, seismic wave speeds, and H<sub>2</sub>O contents. *J. Geophys. Res. Solid Earth* **2003**, *108*, 2029. [[CrossRef](#)]
- Abers, G.A.; Nakajima, J.; van Keken, P.E.; Kita, S.; Hacker, B.R. Thermal–petrological controls on the location of earthquakes within subducting plates. *Earth Planet. Sci. Lett.* **2013**, *369–370*, 178–187. [[CrossRef](#)]
- Rubie, D.C. Role of kinetics in the formation and preservation of eclogites. In *Eclogite Facies Rocks*; Carswell, D.A., Ed.; Springer: Dordrecht, The Netherlands, 1990; pp. 111–140.
- Hernández-Urbe, D.; Palin, R.M. A revised petrological model for subducted oceanic crust: Insights from phase equilibrium modelling. *J. Metamorph. Geol.* **2019**, *37*, 745–768. [[CrossRef](#)]

15. Groppo, C.; Lombardo, B.; Castelli, D.; Compagnoni, R. Exhumation history of the UHPM Brossasco-Isasca unit, Dora-Maira massif, as inferred from a phengite-amphibole eclogite. *Int. Geol. Rev.* **2007**, *49*, 142–168. [[CrossRef](#)]
16. Massonne, H.-J. Formation of amphibole and clinozoisite-epidote in eclogite owing to fluid infiltration during exhumation in a subduction channel. *J. Petrol.* **2012**, *53*, 1969–1998. [[CrossRef](#)]
17. Palin, R.M.; St-Onge, M.; Waters, D.J.; Searle, M.P.; Dyck, B. Phase equilibria modelling of retrograde amphibole and clinozoisite in mafic eclogite from the Tso Morari massif, northwest India: Constraining the P–T–M(H<sub>2</sub>O) conditions of exhumation. *J. Metamorph. Geol.* **2014**, *32*, 675–693. [[CrossRef](#)]
18. Austrheim, H. Eclogitisation of lower crustal granulites by fluid migration through shear zones. *Earth Planet. Sci. Lett.* **1987**, *81*, 221–232. [[CrossRef](#)]
19. Barnicoat, A.C. The mechanism of veining and retrograde alteration of Alpine eclogites. *J. Metamorph. Geol.* **1988**, *6*, 545–558. [[CrossRef](#)]
20. Jamtveit, B.; Bucher-Nurminen, K.; Austrheim, H. Fluid controlled eclogitization of granulites in deep crustal shear zones, Bergen arcs, Western Norway. *Contrib. Mineral. Petrol.* **1990**, *104*, 184–193. [[CrossRef](#)]
21. Yardley, B.W.D. The evolution of fluids through the metamorphic cycle. In *Fluid Flow and Transport in Rocks*; Jamtveit, B., Yardley, B.W.D., Eds.; Chapman & Hall: London, UK, 1997; pp. 99–117.
22. Glodny, J.; Austrheim, H.; Molina, J.F.; Rusin, A.I.; Seward, D. Rb/Sr record of fluid-rock interaction in eclogites: The Marun-Keu complex, Polar Urals, Russia. *Geochim. Cosmochim. Acta* **2003**, *67*, 4353–4371. [[CrossRef](#)]
23. de Sigoyer, J.; Guillot, S.; Lardeaux, J.-M.; Mascle, G. Glaucophane-bearing eclogites in the Tso Morari dome (eastern Ladakh, NW Himalaya). *Eur. J. Mineral.* **1997**, *9*, 1073–1083. [[CrossRef](#)]
24. de Sigoyer, J.; Chavagnac, V.; Blichert-Toft, J.; Villa, I.M.; Luais, B.; Guillot, S.; Cosca, M.; Mascle, G. Dating the Indian continental subduction and collisional thickening in the northwest Himalaya: Multichronology of the Tso Morari eclogites. *Geology* **2000**, *28*, 487–490. [[CrossRef](#)]
25. St-Onge, M.R.; Rayner, N.; Palin, R.M.; Searle, M.P.; Waters, D.J. Integrated pressure-temperature-time constraints for the Tso Morari dome (NW India): Implications for the burial and exhumation path of UHP units in the western Himalaya. *J. Metamorph. Geol.* **2013**, *31*, 469–504. [[CrossRef](#)]
26. Skuzovatov, S.Y.; Wang, K.-L.; Shatsky, V.S.; Buslov, M.M. Geochemistry, zircon U-Pb age and Hf isotopes of the North Muya block granitoids (Central Asian Orogenic belt): Constraints on petrogenesis and geodynamic significance of felsic magmatism. *Precambrian Res.* **2016**, *280*, 14–30. [[CrossRef](#)]
27. Skuzovatov, S.Y.; Wang, K.-L.; Dril, S.I.; Lee, H.-Y.; Iizuka, Y. Geochemistry, zircon U-Pb and Lu-Hf systematics of high-grade metasedimentary sequences from the South Muya block (northeastern Central Asian Orogenic Belt): Reconnaissance of polymetamorphism and accretion of Neoproterozoic exotic blocks in southern Siberia. *Precambrian Res.* **2019**, *321*, 34–53.
28. Skuzovatov, S.Y.; Shatsky, V.S.; Wang, K.-L. Continental subduction during arc-microcontinent collision in the southern Siberian craton: Constraints on protoliths and metamorphic evolution of the North Muya complex eclogites (Eastern Siberia). *Lithos* **2019**, *342–343*, 76–96. [[CrossRef](#)]
29. Bulgatov, A.N. *Tectonotype of Baikals; Nauka: Novosibirsk, Russia, 1983; 193p.* (In Russian)
30. Bulgatov, A.G.; Gordienko, I.V. Terranes of the Baikal mountainous region and location of gold deposits. *Geol. Ore Depos.* **1999**, *41*, 230–240. (In Russian)
31. Salop, L.I. *Geology of Baikal Mountain Area; Nedra: Moscow, Russia, 1964; 517p.* (In Russian)
32. Rytsk, E.Y.; Amelin, Y.V.; Rizvanova, N.G.; Krinsky, R.S.; Mitrofanov, G.L.; Mitrofanova, N.N.; Perelyaev, V.I.; Shalaev, V.S. Age of Rocks in the Baikal-Muya Foldbelt. *Stratigr. Geol. Correl.* **2001**, *9*, 3–15.
33. Mitrofanov, G.L. Evolution of tectonic structures and stages of the continental crust formation of North-Western Transbaikalia. In *Tectonics and Metallogeny of Eastern Siberia*; Irkutsk State University: Irkutsk, Russia, 1978; pp. 38–56. (In Russian)
34. Rytsk, E.Y.; Kovach, V.P.; Yarmolyuk, V.V.; Kovalenko, V.I. Structure and evolution of the continental crust in the Baikal Fold Region. *Geotectonics* **2007**, *41*, 440–464. [[CrossRef](#)]
35. Shatsky, V.S.; Malkovets, V.G.; Belousova, E.A.; Skuzovatov, S.Y. Evolution history of the Neoproterozoic eclogite-bearing complex of the Muya dome (Central Asian Orogenic Belt): Constraints from zircon U-Pb age, Hf and whole-rock Nd isotopes. *Precambrian Res.* **2015**, *261*, 1–11. [[CrossRef](#)]
36. Skuzovatov, S.Y.; Sklyarov, E.V.; Shatsky, V.S.; Wang, K.-L.; Kulikova, K.V.; Zarubina, O.V. Granulites of the South-Muya block (Baikal-Muya Foldbelt): Age of metamorphism and nature of protolith. *Russ. Geol. Geophys.* **2016**, *57*, 451–463. [[CrossRef](#)]
37. Skuzovatov, S.Y.; Shatsky, V.S.; Dril, S.I. High-pressure mafic granulites of the South Muya block (Central Asian Orogenic Belt). *Doklady Earth Sci.* **2017**, *473*, 423–426. [[CrossRef](#)]
38. Shatsky, V.S.; Sitnikova, E.S.; Tomilenko, A.A.; Ragozin, A.L.; Koz'menko, O.A.; Jagoutz, E. Eclogite-gneiss complex of the Muya block (East Siberia): Age, mineralogy, geochemistry, and petrology. *Russ. Geol. Geophys.* **2012**, *53*, 501–521. [[CrossRef](#)]
39. Shatskii, V.S.; Skuzovatov, S.Y.; Ragozin, A.L.; Dril, S.I. Evidence of Neoproterozoic continental subduction in the Baikal-Muya fold belt. *Doklady Earth Sci.* **2014**, *495*, 1442–1445. [[CrossRef](#)]
40. Brandelik, A. CALCMIN—An EXCEL (TM) Visual Basic application for calculating mineral structural formulae from electron microprobe analyses. *Comput. Geosci.* **2009**, *35*, 1540–1551. [[CrossRef](#)]
41. Holland, T.; Blundy, J. Non-ideal interactions in calcic amphiboles and their bearing on amphibole-plagioclase thermometry. *Contrib. Mineral. Petrol.* **1994**, *116*, 433–447. [[CrossRef](#)]

42. Connolly, J.A.D. Computation of phase equilibria by linear programming: A tool for geodynamic modeling and its application to subduction zone decarbonation. *Earth Planet. Sci. Lett.* **2005**, *236*, 524–541. [[CrossRef](#)]
43. Holland, T.J.B.; Powell, R. An internally-consistent thermodynamic dataset for phases of petrological interest. *J. Metamorph. Geol.* **1998**, *16*, 309–344. [[CrossRef](#)]
44. White, R.W.; Powell, R.; Holland, T.J.B. Progress relating to calculation of partial melting equilibria for metapelites. *J. Metamorph. Geol.* **2007**, *25*, 511–527. [[CrossRef](#)]
45. Green, E.C.R.; Holland, T.J.B.; Powell, R. An order-disorder model for omphacitic pyroxenes in the system jadeite-diopside-hedenbergite-acmite, with applications to eclogite rocks. *Am. Mineral.* **2007**, *92*, 1181–1189. [[CrossRef](#)]
46. Dale, J.; Powell, R.; White, R.W.; Elmer, F.L.; Holland, T.B.J. A thermodynamic model for Ca–Na clinoamphiboles in Na<sub>2</sub>O–CaO–FeO–MgO–Al<sub>2</sub>O<sub>3</sub>–SiO<sub>2</sub>–H<sub>2</sub>O–O for petrological calculations. *J. Metamorph. Geol.* **2005**, *23*, 771–791. [[CrossRef](#)]
47. Holland, T.; Powell, R. A Compensated-Redlich-Kwong (CORK) equation for volumes and fugacities of CO<sub>2</sub> and H<sub>2</sub>O in the range 1 bar to 50 kbar and 100–1600 °C. *Contrib. Mineral. Petrol.* **1991**, *109*, 265–273. [[CrossRef](#)]
48. Leake, B.E.; Woolley, A.R.; Arps, C.E.S.; Birch, W.D.; Gilbert, M.C.; Grice, J.D.; Hawthorne, F.C.; Kato, A.; Kisch, H.J.; Krivovichev, V.G.; et al. Nomenclature of amphiboles: Report of the subcommittee on amphiboles of the International Mineralogical Association commission on new minerals and mineral names. *Mineral. Mag.* **1997**, *61*, 295–321. [[CrossRef](#)]
49. Hawthorne, F.C.; Oberti, R.; Harlow, G.E.; Maresch, W.V.; Martin, R.F.; Schumacher, J.C.; Welch, M.D. Nomenclature of the amphibole supergroup. *Am. Mineral.* **2012**, *97*, 2031–2048. [[CrossRef](#)]
50. Li, J.-L.; Klemm, R.; Gao, J.; Jiang, T.; Song, Y.-H. A common high-pressure metamorphic evolution of interlayered eclogites and metasediments from the ‘ultrahigh-pressure unit’ of the Tianshan metamorphic belt in China. *Lithos* **2015**, *226*, 169–182. [[CrossRef](#)]
51. Viete, D.R.; Hacker, B.R.; Allen, M.B.; Seward, G.G.E.; Tobin, M.J.; Kelley, C.S.; Cinque, G.; Duckworth, A.R. Metamorphic records of multiple seismic cycles during subduction. *Sci. Adv.* **2018**, *4*, eaaq0234. [[CrossRef](#)]
52. Carlson, W.D. Rates of Fe, Mg, Mn, and Ca diffusion in garnet. *Am. Mineral.* **2006**, *91*, 1–11. [[CrossRef](#)]
53. Kelley, K.A.; Cottrell, E. Water and the oxidation state of subduction zone magmas. *Science* **2009**, *325*, 605–607. [[CrossRef](#)]
54. Heinrich, C.A. Kyanite-eclogite to amphibolite facies evolution of hydrous mafic and pelitic rocks, Adula nappe, Central Alps. *Contrib. Mineral. Petrol.* **1982**, *81*, 30–38. [[CrossRef](#)]
55. Yardley, B.W.D.; Baltatzis, E. Retrogression of staurolite schists and the sources of infiltrating fluids during metamorphism. *Contrib. Mineral. Petrol.* **1985**, *89*, 59–68. [[CrossRef](#)]
56. Rubie, D.C. The catalysis of mineral reactions by water and restrictions on the presence of aqueous fluid during metamorphism. *Mineral. Mag.* **1986**, *50*, 399–415. [[CrossRef](#)]
57. Molina, J.F.; Austrheim, H.; Glodny, J.; Rusin, A. The eclogites of the Marun-Keu Complex (Polar Urals, Russia). *Lithos* **2002**, *61*, 55–78. [[CrossRef](#)]
58. Guiraud, M.; Powell, R.; Rebay, G. H<sub>2</sub>O in metamorphism and unexpected behaviour in the preservation of metamorphic mineral assemblages. *J. Metamorph. Geol.* **2001**, *19*, 445–454. [[CrossRef](#)]
59. Martin, C.; Duchêne, S. Residual water in hydrous minerals as a kinetic factor for omphacite destabilization into symplectite in the eclogites of Vårdalsneset (WGR, Norway). *Lithos* **2015**, *232*, 162–173. [[CrossRef](#)]
60. Spear, F.S. *Metamorphic Phase Equilibria and Pressure-Temperature-Time-Paths*; Mineralogical Society of America: Chantilly, VA, USA, 1993; 799p, ISBN 0-939950-34-0.
61. Avchenko, O.V.; Gabov, N.F.; Kozyreva, I.V.; Konikov, A.Z.; Travin, L.V. Composition and origin of eclogites of the North Muya block. *Int. Geol. Rev.* **1995**, *31*, 792–805. [[CrossRef](#)]
62. Manning, C.E. Fluid composition at the blueschist-eclogite transition in the model system Na<sub>2</sub>O–MgO–Al<sub>2</sub>O<sub>3</sub>–SiO<sub>2</sub>–H<sub>2</sub>O–HCl. *Swiss Bull. Mineral. Petrol.* **1998**, *78*, 225–242.
63. Miller, J.A.; Buick, I.S.; Cartwright, I.; Barnicoat, A. Fluid processes during the exhumation of high-P metamorphic belts. *Mineral. Mag.* **2002**, *66*, 93–119. [[CrossRef](#)]
64. Philippot, P.; Selverstone, J. Trace-element-rich brines in eclogitic veins: Implications for fluid composition and transport during subduction. *Contrib. Mineral. Petrol.* **1991**, *106*, 417–430. [[CrossRef](#)]
65. Davies, J.H.; Stevenson, D.J. Physical model of source region of subduction zone volcanics. *J. Geophys. Res.* **1992**, *97*, 2037–2070. [[CrossRef](#)]